Altered firing output of VIP interneurons and early dysfunctions in CA1 hippocampal circuits in the 3xTg mouse model of Alzheimer's disease

Felix Michaud[1,2*], Ruggiero Francavilla[1,2,3*], Dimitry Topolnik[1,2], Parisa Iloun[1,2], Suhel Tamboli[1,2], Frederic Calon[2, 4], Lisa Topolnik[1,2,5]

[1]Department of Biochemistry, Microbiology and Bio-informatics, Laval University, Québec, QC, Canada
[2]Neuroscience Axis, CHU de Québec Research Center (CHUL), Québec, QC, Canada
[3]Present adresse : CHU Sainte-Justine Research Center, Université de Montréal, Montreal, QC, Canada; Department of Neurosciences, Université de Montréal, Montreal, QC, Canada
[4]Faculty of Pharmacy, Laval University, Québec, QC, Canada.
[5]Corresponding author
**These authors contributed equally to this work.*

Significance: This study examines VIP interneurons in the CA1 hippocampus affected by Alzheimer's disease (AD) pathology. While these cells maintain their structural integrity, they exhibit altered firing patterns in young adult 3xTg-AD mice. These changes might correlate with enhanced CA1 inhibition and impact the activation of principal cells. These findings shed light on early dysfunction in hippocampal circuits as a potential mechanism of AD pathology and offer insights into prospective therapeutic targets.

Correspondence should be addressed to:
Dr. Lisa Topolnik
Lisa.topolnik@bcm.ulaval.ca

Abstract

Alzheimer's disease (AD) leads to progressive memory decline, and alterations in hippocampal function are among the earliest pathological features observed in human and animal studies. GABAergic interneurons (INs) within the hippocampus coordinate network activity, among which type 3 interneuron-specific (I-S3) cells expressing vasoactive intestinal polypeptide and calretinin play a crucial role. These cells provide primarily disinhibition to principal excitatory cells (PCs) in the hippocampal CA1 region, regulating incoming inputs and memory formation. However, it remains unclear whether AD pathology induces changes in the activity of I-S3 cells, impacting the hippocampal network motifs. Here, using young adult 3xTg-AD mice, we found that while the density and morphology of I-S3 cells remain unaffected, there were significant changes in their firing output. Specifically, I-S3 cells displayed elongated action potentials and decreased firing rates, which was associated with a reduced inhibition of CA1 INs and their higher recruitment during spatial decision-making and object exploration tasks. Furthermore, the activation of CA1 PCs was also impacted, signifying early disruptions in CA1 network functionality. These findings suggest that altered firing patterns of I-S3 cells might initiate early-stage dysfunction in hippocampal CA1 circuits, potentially influencing the progression of AD pathology.

Introduction

Memory impairments pose a significant burden on individuals grappling with Alzheimer's disease (AD). A series of recent investigations has underscored the pivotal role of hippocampal GABAergic interneurons (INs) in memory dysfunction in AD (Verret et al., 2012; Cattaud et al., 2018; Martinez-Losa et al., 2018; Schmid et al., 2016; Rice et al., 2020; Caccavano et al., 2020; Chung et al., 2020; Hijazi et al., 2020; Algamal et al., 2022; Hernandez-Frausto et al., 2023). Among the various types of hippocampal INs, CA1 parvalbumin- (PV-INs), somatostatin- (SOM-INs), and to a certain extend calretinin- (CR-INs) expressing cells have received significant attention. Postmortem data reveals diminished numbers of SOM-INs in the temporal cortex of AD patients, while the populations of PV-INs and CR-INs remain relatively unaffected (Hof et al., 1993; Brady and Mufson, 1997; Waller et al., 2020). Furthermore, significant synaptic rewiring in SOM-INs due to a decreased cholinergic drive has been documented in mice with AD-like pathology (Schmid et al., 2016). This disturbance has led to memory deficits, underscoring the central role played by SOM-INs in the dysfunction observed in AD (Schmid et al., 2016). Whereas most INs control different stages of hippocampal information processing by providing inhibition to different subcellular domains of principal cells (PCs), a specific population of the vasoactive intestinal polypeptide-expressing cells (VIP-INs) regulates the activity of INs (Acsády et al., 1996b; Tyan et al., 2014; Francavilla et al., 2015; 2018; Luo et al., 2019; 2020; Kullander and Topolnik, 2021). The hippocampal CA1 VIP-INs engage in goal-directed and spatial learning by tuning the activity of principal cells via input-specific disinhibition (Magnin et al., 2019; Turi et al., 2019; Bilash et al., 2023). Specifically, long-range glutamatergic inputs from the lateral entorhinal cortex can recruit VIP-INs to modulate dendritic excitability of CA1 PCs through disinhibition and support contextual memory (Bilash et al., 2023). The role of circuit disinhibition and VIP-INs in the AD pathology remains unknown.

The 3xTg-AD (Tg(APPSwe,tauP301L)1Lfa *Psen1*^{tm1Mpm}/Mmjax) mouse model, combining three familial AD mutations (Swedish *APP* KM670/671NL, *PSEN1* M146V, and *MAPT P301L*) exhibits accumulation of amyloid-β (Aβ)

plaques and neurofibrillary tangles, synaptic impairment, and cognitive deficits (Javonillo et al., 2022). As a result, 3xTg-AD mutant mice have become a primary choice for investigating AD mechanisms (Drummond and Wisniewski, 2017; Myers and McGonigle, 2019). Extensive work employing this model has focused on the CA1 region of the hippocampus, recognized as a central hub for spatial learning and episodic memory (Oddo et al., 2003; Chakroborty et al., 2009; Noristani et al., 2011; Clark et al., 2015; Mably et al., 2017; Stimmel et al., 2019; Javonillo et al., 2022; Lin et al., 2022). In vitro and in vivo studies with 3xTg-AD mutants have provided evidence of disrupted synaptic plasticity in CA1 as one of the earliest signs of pathology. This occurs even before the accumulation of extracellular Aβ plaques and neurofibrillary tangles, which begins at 6 months of age and progresses further after 12 months (Davis et al., 2014; Clark et al., 2015; Javonillo et al., 2022). While CA1 INs are known to play a crucial role in regulating synaptic plasticity, memory encoding, and consolidation (Topolnik and Tamboli, 2022), it is yet unclear whether they undergo early changes in the AD progression. However, there is evidence indicating that mice with overexpression of the amyloid precursor protein (APP) with the Swedish mutation and deltaE9 mutation in presenilin 1 (*APP/PS1*) display reduced activity of CA1 PV-INs but increased activity of SOM-INs (Algamal et al., 2022). This suggests that disrupted communication within local inhibitory circuits may contribute to APP/PS1-mediated memory dysfunction (Palop and Mucke, 2016). Nevertheless, investigations into the activity profiles and local synaptic communication among CA1 INs of 3xTg-AD mice in vivo have been lacking. Importantly, prior studies on aged mice have identified significant changes in firing properties of type 3 interneuron-specific interneurons (I-S3), which co-express CR and VIP and control the activity of SOM-INs but also of PV-INs in the CA1 hippocampal region (Tyan et al., 2014; Francavilla et al., 2020; Luo et al., 2020). Whether impairments in I-S3 activity might contribute to altered CA1 inhibition and network function in 3xTg-AD mice remains unknown.

In this study, we examined IN function in the CA1 region of young adult (P90–260) 3xTg-AD mice. In awake animals, CA1 INs displayed increased activity, specifically during tasks involving spatial decision-making and object exploration.

This increased activity of INs was not a result of changes in the excitatory drive to INs but rather stemmed from a reduced inhibitory tone, indicating impaired inhibition of CA1 INs. Consequently, the firing rate of I-S3 cells, which provide inhibition to CA1 INs, was significantly reduced. At a network level, these alterations in IN function had an impact on the activation of CA1 PCs, the fundamental units for processing information in the hippocampus (Soltesz and Losonczy, 2018). Thus, these early changes may contribute to an imbalance between excitation and inhibition, impairing induction of synaptic plasticity, and ultimately leading to memory dysfunction.

Results

VIP-INs accumulate intracellular Aβ and its precursor at the early stages of AD progression

To examine the properties of VIP/CR-coexpressing I-S3 cells in AD-afflicted mice, we generated VIP-eGFP-3xTg (VIP-Tg) mice by crossing homozygous 3xTg-AD (Tg) with VIP-eGFP (VIP-nonTg) mice, in which all interneurons immunoreactive for VIP express eGFP (Tyan et al., 2014). To pinpoint the stage with initial signs of pathology in these experimental animals, we first assessed Aβ expression in sections from the VIP-Tg animals using the 6E10 antibody which binds to an epitope found in both human APP and Aβ and may detect full-length APP, α-APP (soluble alpha-secretase-cleaved APP), the C-terminal (C99) fragment of APP and Aβ (LaFerla et al., 2007). Consistent with previous findings (Mastrangelo and Bowers, 2008; Davis et al., 2013), we observed widespread intracellular Aβ/APP labelling within the CA1 pyramidal layer from P90, progressing further by P180 (***Figure 1a***; VIP-Tg: n = 8 sections/3 animals; ***Supplementary Table 1***). Moreover, intracellular Aβ/APP accumulation was observed in VIP-INs with soma located within *stratum pyramidale* (PYR) and *stratum radiatum* (RAD) (***Figure 1b***).

At this age, Tg mice are typically considered asymptomatic as they do not show major memory impairments (Pairojana et al., 2021; Javonillo et al., 2022). However, previous reports suggest episodic-like memory deficits in 3-6-month-old Tg mice when using complex tests combining object structure, location, and

context for assessment of recognition memory (Davis et al., 2013; 2014). To examine whether this applies to VIP-Tg animals, we compared the performance of VIP-nonTg versus VIP-Tg animals in the object-place test (OPT; ***Figure 1—figure supplement 1a, b***; VIP-nonTg: n = 10 mice; VIP-Tg: n = 11 mice; ***Supplementary Table 1***) (Francavilla et al., 2020), and observed a significant impairment in the recognition index (RI) for novel object. Notably, the total object exploration time and the overall animal activity didn't significantly differ between the two mouse lines (***Figure 1—figure supplement 1c***; VIP-nonTg: n = 10 mice; VIP-Tg: n = 11 mice; ***Supplementary Table 1***), suggesting that the lower RI in VIP-Tg mice is associated with early deficits in novelty recognition rather than decreased exploratory behavior. These findings indicate that VIP-Tg mice show initial signs of AD-related pathology with intracellular Aβ accumulation in PCs and VIP-INs, along with associated deficits in episodic-like memory starting from P90. Accordingly, for I-S3 analysis, we selected mice aged between P90 to P180 (n = 27).

To explore the potential loss of CA1 VIP interneurons in VIP-Tg mice, we conducted immunohistochemistry on hippocampal slices from both VIP-nonTg and VIP-Tg mice (***Figure 1c, d; Supplementary Table 1***). We observed no alteration in the density of VIP-INs within the CA1 region (***Figure 1c, d***; VIP-nonTg: n = 17 sections/3 animals; VIP-Tg: n = 13 sections/3 animals), suggesting that this interneuronal population persists in VIP-Tg mice. Additionally, our findings revealed no disparity in either CR-INs or VIP subtype co-expressing CR and VIP and representing the I-S3 cells (***Figure 1c, d***; VIP-nonTg: n = 11 sections/3 animals; VIP-Tg: n = 11 sections/3 animals), although a significant loss of I-S3 cells was apparent when removing the outlier (Wilcoxon rank test, p = 0.0193; VIP-nonTg n = 11 sections/3 animals; VIP-Tg: n = 10 sections/3 animals). This indicates that I-S3 cells still survive in young VIP-Tg mice but their density tends to decrease upon pathology progress.

I-S3 cells exhibit wider spikes but lower firing rate in VIP-Tg mice

Given that AD pathology can influence the firing behavior of hippocampal neurons (Vitale et al., 2021; Rowan et al., 2022), we proceeded with targeted patch-clamp recordings from I-S3 cells to compare their passive and active membrane properties in slices obtained from VIP-nonTg and VIP-Tg mice (***Figure 2***). Notably, the resting membrane potential, input resistance, membrane capacitance and membrane time constant of I-S3 cells showed no significant differences between VIP-nonTg (–60.5 ± 1.7 mV, 517 ± 37 MΩ, 32.8 ± 3.5 pF, 36.5 ± 3.2 ms) and VIP-Tg mice (–65.8 ± 2.1 mV, 493 ± 45 MΩ, 29.3 ± 2.9 pF, 35.7 ± 2.2 ms), respectively (***Figure 2a–c***; VIP-nonTg: n = 8 cells/5 animals; VIP-Tg: n = 10 cells/3 animals). However, distinct alterations were evident in firing and AP properties (***Figure 2***). Specifically, I-S3 cells in VIP-Tg animals exhibited a significant increase in AP half-width and area, along with a slower AP repolarization phase compared to VIP-nonTg mice (***Figure 2a–c***; VIP-nonTg: n = 8 cells/5 animals; VIP-Tg: n = 10 cells/3 animals; ***Supplementary Table 1***). Moreover, at a 2x rheobase current during the firing train, although the AP amplitude was lower in VIP-Tg mice, the prolonged AP half-width resulted in an increased AP area (***Figure 2d***; VIP-nonTg: n = 7 cells/5 animals; VIP-Tg: n = 7 cells/3 animals; ***Supplementary Table 1***). The elongated AP duration linked to a slower AP repolarization rate led to a reduced firing rate of I-S3 cells in VIP-Tg animals (***Figure 2e, f***; VIP-nonTg: n = 7 cells/5 animals; VIP-Tg: n = 7 cells/3 animals; ***Supplementary Table 1***). Collectively, these findings highlight specific alterations in the firing output of I-S3 interneurons, characterized by prolonged individual spikes and reduced firing frequency in the early stages of AD pathology.

To investigate whether alterations in physiological properties extend to changes in synaptic input that I-S3 cells receive, we conducted recordings of sIPSCs and sEPSCs in slices from VIP-nonTg and VIP-Tg mice (***Figure 2—figure supplement 2***). However, our findings revealed no significant difference in either the amplitude or frequency of sIPSCs (***Figure 2—figure supplement 2a–c***; VIP-nonTg: n = 7 cells/5 animals; VIP-Tg: n = 6 cells/5 animals; ***Supplementary Table 1***). Likewise, both the amplitude and frequency of sEPSCs displayed no noticeable changes (***Figure 2—figure supplement 2a–c***; VIP-nonTg: n = 5 cells/5 animals;

VIP-Tg: n = 4 cells/4 animals; ***Supplementary Table 1***). Consequently, these results suggest that the synaptic inputs to I-S3 cells remain unaffected in VIP-Tg mice.

Given the potential for hippocampal CR-INs to exhibit abnormal morphology characterized by prominent dystrophic neurites due to Aβ accumulation (Baglietto-Vargas et al., 2010), we also investigated the morphological properties of anatomically confirmed I-S3 interneurons reconstructed in Neurolucida (***Figure 2—figure supplement 3***). However, our analysis revealed no variations in the morphology of I-S3 cells. Specifically, there were no differences observed in soma area, dendritic surface, total dendritic length, or the number of branching points (***Figure 2—figure supplement 3b–e***; VIP-nonTg: n = 6 cells/5 mice; VIP-Tg: n = 5 cells/4 mice; ***Supplementary Table 1***). Moreover, the dendritic Sholl analysis displayed no disparities in the number of dendritic intersections, dendritic length or the number of dendritic nodes at various distances from the soma (***Figure 2—figure supplement 3f***; VIP-nonTg: n = 5 cells/5 mice; VIP-Tg: n = 5 cells/4 mice). These findings suggest that I-S3 cells only modify their firing properties in VIP-Tg mice without significant alteration in other cellular parameters.

Altered inhibitory drive to O/A interneurons in Tg mice: impact of I-S3 cell firing patterns

To examine whether the modified firing properties of I-S3 cells could impact the inhibitory drive to their postsynaptic targets – distinct types of O/A INs (Tyan et al., 2014), we conducted recordings of sIPSCs in O/A INs (***Figure 3a–c***; nonTg: n = 16 cells/5 animals; Tg: n = 10 cells/4 animals). Among recorded cells, both OLM and bistratified cells, the main targets of I-S3 cells, were identified using biocytin staining. These data revealed no significant change in the amplitude of sIPSCs, but a reduction in the frequency of sIPSCs events in the Tg group (***Figure 3b; Supplementary Table 1***). Moreover, our data indicated increased rise and decay time constant of sIPSCs, consequently enhancing the charge transfer (***Figure 3c; Supplementary Table 1***) in the Tg group.

To explore whether the decreased frequency of inhibitory events in O/A INs might be linked to a loss of synaptic contacts from I-S3 cells, we examined the density of inhibitory axonal boutons labelled with vesicular GABA transporter (VGAT) and CR within CA1 O/A of both groups (***Figure 3d, e***; nonTg: n = 19 sections/4 animalsTg: n = 21 sections/4 animals). However, the data showed no alteration in either VGAT or VGAT-CR boutons between the two groups (***Figure 3e;*** **Supplementary Table 1**). We also examined potential changes in the excitatory drive to O/A INs by recording sEPSCs but found no disparities in the amplitude, frequency or kinetics of those currents between Tg and nonTg animals (***Figure 3—figure supplement 4a–c***; nonTg: n = 8 cells/5 animals; Tg: n = 5 cells/4 animals; ***Supplementary Table 1***). Collectively, these data indicate, that CA1 interneurons in Tg mice exhibit a modified inhibitory input characterized by slower kinetics and reduced frequency of inhibitory currents. Moreover, these alterations weren't a result of modified synaptic connectivity but rather seemed originated from specific changes in the firing output of I-S3 cells, characterized by slower APs and a decreased firing rate.

Enhanced IN activity during cognitive tasks in Tg mice

To explore whether alterations in the inhibitory drive received by CA1 INs could influence their engagement during behavior, we monitored interneuronal activity during spatial navigation and object encoding. We performed wireless fiber photometry within the CA1 region of the hippocampus in homozygous Tg mutant mice (n = 13) and their non-Tg littermates (n = 13) while they were awake in their home cages, the T-maze or the open field maze (OFM) (***Figure 4—figure supplement 5***). The Dlx-driven expression of GCaMP6f allowed us to assess the activity of both PV-IN and SOM-IN types – the main targets of I-S3 interneurons. Given the fiber properties (core: 400 μm; NA: 0.39), the signal was collected from all INs situated within *stratum oriens/alveus* (O/A) and PYR of the CA1 region (Pisano et al., 2019; Montinaro et al., 2021).

We observed no changes in the overall behavior of the animals or the activity of INs in either the home cage (nonTg: n = 9 animals; Tg: n = 8 animals) or OFM (nonTg: n = 13 animals; Tg: n = 13 animals) in Tg-mutant mice (***Figure 4c,***

Figure 4—figure supplement 5 a–d; Supplementary Table 1) and no changes in their mobility during the T-maze exploration (***Figure 4—figure supplement 5e, f;*** nonTg: n = 10 animals; Tg: n = 5 animals; ***Supplementary Table 1***). Consistent with previous findings highlighting speed modulation of SOM-INs, PV-INs and VIP-INs during locomotion (Arriaga and Han, 2017; Francavilla et al., 2019; Turi et al., 2019; Luo et al., 2020; Geiller et al., 2020), INs exhibited heightened activity during walk, but this pattern of activity remained unaffected when comparing nonTg and Tg mice (***Figure 4d, e***; ; nonTg: n = 9 animals; Tg: n = 8 animals; ***Supplementary Table 1***). However, during a decision-making spatial task in a T-maze (***Figure 4f***), both groups performed well (***Figure 4g***; nonTg: n = 9 animals; Tg: n = 6 animals; ***Supplementary Table 1***), yet activity of INs in Tg-mutants notably surged, particularly in the decision zone (D-zone) compared to the stem (***Figure 4h***; nonTg: n = 5 animals; Tg: n = 5 animals; ***Supplementary Table 1***), although the magnitude of change between the DZ and the stem remained unaltered (***Supplementary Table 1***). Similarly, heightened activity of INs was observed in Tg mice during object exploration in the OFM (***Figure 4j***; nonTg: n = 10 animals; Tg: n = 9 animals; ***Supplementary Table 1***), despite no alterations in the number of entries in the objects' zones or in objects' exploration time (***Figure 4i***; nonTg: n = 10 animals; Tg: n = 8 animals; ***Supplementary Table 1***). Consequently, these data indicate that a mouse model carrying three familial AD mutations displays an early-age increase in the activity of hippocampal CA1 INs specifically during cognitive tasks associated with spatial decision-making and object encoding.

Task-dependent modulation of CA1 PC activity in Tg mice

Ultimately, to explore whether changes in activity of CA1 INs influence the recruitment of PCs during behavioral tasks, we monitored the activation of CA1 PC using the CaMKII-promoter-driven GCaMP6f expression (***Figure 5a***; nonTg: n = 4 animals; Tg: n = 5 animals). Similar to INs, no alterations were observed in the baseline activity of PCs when mice were in their homecages; both the amplitude and frequency of calcium transients remained unaltered between Tg and nonTg animals (***Figure 5b; Supplementary Table 1***). Moreover, there was no discernible

change in PCs' activity between the two groups during locomotion in the OFM (***Figure 5c, d***; ***Supplementary Table 1***). However, during spatial decision-making in the T-maze, nonTg mice displayed a consistent increase in PC recruitment specifically within the D-zone. In contrast, Tg mice showed no change in PC activity in this area (***Figure 5e, f; Supplementary Table 1***), consistent with the heightened activity observed in INs in D-zone for Tg mice (***Figure 4h***). Furthermore, during exploration of two different objects, while overall PC activity showed no difference between the two groups (***Figure 5h; Supplementary Table 1***), the object modulation variance was reduced in Tg mice, revealing greater uniformity in signal during object sampling (***Figure 5g, h; Supplementary Table 1***). Collectively, these findings reveal the task-dependent shifts in PCs' recruitment in Tg mice, with unaltered activity during basal routine behavior and task-specific changes during spatial decision-making and object encoding.

Discussion

In this study, we provide novel insights into the early alterations in the physiological properties of I-S3 cells in mice afflicted with AD neuropathology, along with the potential impact of these changes on the recruitement of the CA1 INs and PCs. Our findings indicate that at early stages in AD progression, APP/Aβ is detected intracellularly in I-S3 cells but they maintain their structural integrity. Notably, different subtypes of INs exhibit varying susceptibilities to AD-related pathologies (Ali et al., 2023), with CR-INs displaying anatomical resilience to pathological Aβ accumulation (Shi et al., 2020). This resilience in CR-INs, particularly in the early stages of AD, could be attributed to their ability to counteract Aβ-induced excitotoxicity by restricting cytosolic calcium elevations due to CR expression (Mikkonen et al., 1999; Bezprozvanny and Mattson, 2008; Ali et al., 2023). However, studies have demonstrated the toxicity of the intracellular accumulation of Aβ oligomers (Li et al., 2009; Busche et al., 2012) and their precursors (Mondragón-Rodríguez et al., 2018; Takasugi et al., 2023), highlighting how this may alter cellular processes and circuit function. For example, C99 fragments, which accumulate in 3-month-old 3xTg-AD mice (Lauritzen et al., 2012), are

involved in the regulation of voltage-gated potassium channels of the Kv7 family (Manville and Abbott, 2021). Such a mechanism could modify the firing properties of affected neurons and may be at play in I-S3 cells of 3xTg-AD mice.

Notably, we observed significant alterations in the firing properties of I-S3 cells, characterized by a decrease in AP firing rate, potentially contributing to the heightened activity of O/A INs in specific tasks in freely behaving Tg mice. Functional changes in the neuronal circuits of the hippocampus have been widely recognized in animal models of AD (Busche et al., 2016; Harris et al., 2020). During the initial stages of the disease, there have been reports of hyperexcitability in the hippocampus and medial entorhinal cortex (MEC) (Busche et al., 2008; Busche et al., 2012; Davis et al., 2014; Lin et al., 2022; Chen et al., 2023), consistent with the increased susceptibility to epileptic seizures observed in both animal models and human patients (Palop and Mucke, 2009; Cretin et al., 2016). By providing disinhibition to principal excitatory cells of CA1, I-S3 cells are well positionned to coordinate hippocampal activity levels. Accordingly, in young adult 3xTg-AD mice, the altered firing of I-S3 cells might lead to abnormal disinhibition of PCs, thereby shifting the excitation/inhibition levels and affecting overall network activity. However, our observations revealed more intricate alterations in the output of I-S3 cells, characterized by slower individual APs and a decreased firing rate. The slower repolarization rate in I-S3 cells might arise from intrinsic changes involving Kv3.1 or Kv4.3 subunits expressed by I-S3 cells (Guet-McCreight et al., 2016), which have been suggested to occur during aging in I-S3 cells (Francavilla et al., 2019). Altered Kv3 properties reduce the excitability of cortical PV-INs and contribute to early AD-related network hyperexcitability (Olah et al., 2022). Moreover, increased intrinsic excitability exacerbated by enhanced synaptic inputs has been recently shown in MEC stellate cells in 3-month-old 3xTg-AD mice (Chen et al., 2023). Whether these simultaneous excitability changes in different cell types are initiated by the early intracellular Aβ accumulation or alterations in network activity remains to be determined, but collectively they can contribute to the onset of cognitive deficits. These early cell-type-specific excitability changes might also act as a compensatory mechanism to offset the altered connectivity

motifs in order to normalize the network activity across different areas of the limbic system.

Furthermore, our in vivo data highlights task-specific alterations in the recruitment of CA1 O/A INs, which are the main target of I-S3 cells (Tyan et al., 2014), during spatial navigation and object encoding. If the behavioral task-dependent shifts in the recruitment of O/A INs are associated with alterations in I-S3 excitability, they should be most pronounced during tasks that notably elevate the I-S3 cells' activity. I-S3 cells are engaged in spatial decision-making, object coding and goal-directed behavior (Magnin et al., 2019; Turi et al., 2019; Tamboli et al., 2024). Consistent with the enhanced recruitment of these cells in the D-zone during spatial navigation and their positive modulation by objects (Tamboli et al., 2024), the activity of O/A INs was specifically enhanced during these behavioral patterns. Conversely, while I-S3 cells are modulated by animal running speed (Turi et al., 2019; Luo et al., 2020), no discernible alterations in the activity of O/A INs were noted during walking periods. This is likely due to an overall lower animal speed during free walks in the open arena when compared to treadmill runs (Turi et al., 2019; Luo et al., 2020).

What could be the consequences on memory formation if there are changes in the recruitment of CA1 INs? The task-dependent increase in the activity of SOM-INs, the primary target of I-S3 cells, might lower dendritic excitability of CA1 PCs, impeding their input integration and burst firing (Lovett-Barron et al., 2012; Royer et al., 2012; Tyan et al., 2014; Bilash et al., 2023). This could potentially result in inadequate recruitment of CA1 PCs during decision-making or object sampling tasks. Indeed, our study reveals a decreased recruitment of CA1 PCs within the D-zone of the T-maze and their more uniform activation when exploring different objects. This aligns with increased inhibition and compromised integration of distinct sensory experiences (Inayat et al., 2023). Additionally, both in humans and in animal models of AD, early deficits in network oscillations have been documented (Adler et al., 2003; Herrmann and Demiralp, 2005; van der Hiele et al., 2007; Czigler et al., 2008; Moretti et al., 2010; Scott et al., 2012; Goutagny et al., 2013; Schneider et al., 2014; Jones et al., 2019). Theta oscillations, crucial for

memory formation, are shaped by the recruitment of I-S3 cells (Tyan et al., 2014; Luo et al., 2020). Moreover, OLM cells, a primary target of I-S3 cells, play a significant role in generating theta oscillations (Chatzikalymniou and Skinner, 2018; Mikulovic et al., 2018; Gu et al., 2020). Changes in AP kinetics and firing rate of I-S3 cells could lead to aberrant activation of OLM cells (Tyan et al., 2014), potentially contributing to the early deficits in theta rhythms observed in human cases and AD animal models (Goutagny and Krantic, 2013; Wirt et al., 2021). This hypothesis could be further explored by imaging the activity levels of specific INs types, including OLMs, and their correlation with I-S3 activity during network oscillations and learning tasks in 3xTg-AD mice (Luo et al., 2020; Geiller et al., 2020). It is possible that alterations in interactions between I-S3 cells and their targets shift CA1 disinhibition necessary for sensory integration and decision-making (Geiller et al., 2020; Bilash et al., 2023) towards inhibition, impacting memory encoding dynamics and memory content, particularly in the early stages of AD progression. Understanding these deficits in specific circuit patterns tied to network states could pave the way to novel therapeutic approaches, focussing on early interventions and targeting precise circuit motifs to restore memory function.

Materials and methods

Mouse lines

All experiments were conducted in accordance with the Animal Protection Committee of Université Laval and the Canadian Council on Animal Care. This study involved VIP-eGFP [MMRRC strain #31009, STOCK Tg(Vip-EGFP)37Gsat, University of California, Davis, CA, USA], 3xTg-AD [MMRRC strain #034830-JAX, STOCK B6;129-Tg(APPSwe,tauP301L)1Lfa *Psen1*^{tm1Mpm}/Mmjax] and VIP-eGFP-3xTg (VIP-Tg) mouse lines. Triple-transgenic 3xTg-AD (Tg) mice (APPswe, PSIMI46V, tauP301L) (Oddo et al., 2003) were maintained in our animal facilities and backcrossed every seven to ten generations to C57BL6/129SvJ mice. VIP-Tg mice were generated through breeding homozygous Tg with heterozygous VIP-eGFP ones. The control groups comprised VIP-eGFP mice (VIP-nonTg) of the appropriate age (***Figures 1 and 2***) or non-transgenic littermates from the 3xTg-AD

line (nonTg) (***Figures 3 to 5***). All experiments involved mice (P90–260) of both sexes, equally distributed across each experimental group.

Behavior assays

General exploratory activity in the open field and the object recognition memory of VIP-Tg and VIP-nonTg mice were assessed using the automated VersaMax Animal Activity Monitoring System (AccuScan Instruments, Columbus, OH). The open field was a square arena (20 x 20 x 30.5 cm) made of plexiglass equipped with photocell beams for automatic detection of activity. On day 1 mice were placed in the open field maze (OFM) to explore it for 5 minutes (***Figure supplement 1***). The same arena was used for the object-place task (OPT). On day 2, during the Sample phase, mice were placed in the OFM with two different sample objects (A + B; 4 x 4 cm each) for 5 min, after which they were returned to their home cage for 24-hours retention interval. On day 3, during the Test phase, mice re-entered the arena with two objects, one was identical to the Sample phase and the other was novel (C + A; 4 x 4 cm each). As 3xTg-AD mice at this age do not typically show deficits in novel-object-recognition test (Pairojana et al., 2021), to add the complexity to this test, we altered the spatial location of the familiar object explored by the mouse. The results are expressed as a Recognition Index (RI, %), defined as the ratio of the time spent with new object divided by the total exploration time for novel and familiar objects [RI = $(T_N)/(T_N + T_F)$]. An exploration time was also calculated for the time spent with the two objects in the Test phase ($ET_T = T_N + T_F$). Control mice show preference for a novel object in this test (Francavilla et al., 2020).

To investigate object modulation of neuronal activity, another group of mice were positioned in a rectangular arena (36 x 29 x 21.5 cm) made of opaque plastic equipped with video camera for automatic detection of activity. The animal activity (immobility, locomotion and rearing periods) was monitored using the AnyMaze software. Animal tracking was performed using the ToxTrac software v2.96 (Rodriguez, 2018) to assess speed, mobility rate and distance traveled. Two

identical objects (A + A; 4 x 4 cm each) were used for object modulation assessment.

T-maze was performed in a T-shaped plexiglass maze (80 x 68 x 15 cm). A single mouse was placed at the beginning of the maze and restricted manually to the selected arm for 30 seconds using a cardboard door. The mouse was then repositioned at the beginning and left to explore for a total trial duration of 5 min. To assess spatial memory, selected arm alternation was measured. To measure calcium activity during decision making periods, a decision zone was defined as the square area located at the intersection of the maze (***Figure 4f***). Between animals the arena and objects were cleaned with 70% ethanol.

We excluded from the analysis the animals that refused to explore the T-maze and spent all their time in the stem corner, or refused to explore the objects and stayed in the OFM corner. These exclusions applied to both non-Tg (n = 6 mice) and Tg (n = 5 mice) groups, indicating that low exploratory activity is not necessarily linked to AD-related mutations. During the T-maze test, we also observed several animals that made incorrect choices (4 out of 9 non-Tg and 1 out of 6 Tg mice). However, due to the low number of animals making incorrect choices, we were unable to form a separate group for analysis based on incorrect choices.

Slice preparation and patch-clamp recordings

Transversal hippocampal slices (thickness, 300 µm) were prepared from VIP-nonTg, VIP-Tg, nonTg or Tg mice of either sex. The animals were anesthetized with ketamine-xylazine mixture (10/100 mg/ml), transcardially perfused with 20 mL of ice-cold sucrose-based cutting solution (containing the following in mM: 250 sucrose, 2 KCl, 1.25 NaH_2PO_4, 26 $NaHCO_3$, 7 $MgSO_4$, 0.5 $CaCl_2$, and 10 glucose, pH 7.4, 330–340 mOsm/L) and decapitated (David and Topolnik, 2017). Slices were cut in the cutting solution using a vibratome (VT1000S; Leica Microsystems or Microm; Fisher Scientific), and transferred to a heated (37.5°C) oxygenated recovery solution containing the following (in mM): 124 NaCl, 2.5 KCl, 1.25 NaH_2PO_4, 26 $NaHCO_3$, 3 $MgSO_4$, 1 $CaCl_2$, and 10 glucose; pH 7.4; 300 mOsm/L, to recover for at least 45 min. During experiments, slices were continuously perfused (2 mL/min) with standard artificial cerebrospinal fluid (ACSF) containing

the following (in mM): 124 NaCl, 2.5 KCl, 1.25 NaH_2PO_4, 26 $NaHCO_3$, 2 $MgSO_4$, 2$CaCl_2$, and 10 glucose, pH 7.4 saturated with 95% O_2 and 5% CO_2 at near physiological temperature (30–33ºC). VIP-expressing interneurons located in RAD and PYR were visually identified as eGFP-expressing cells under an epifluorescence microscope with blue light (filter set: 450–490 nm). All electrophysiological recordings were carried out using a 40x water-immersion objective. A Flaming/Brown micropipette puller (Sutter Instrument Co.) was used to make patch pipettes (3.5-6 MΩ). Whole-cell patch-clamp recordings from VIP or O/A interneurons were performed in voltage or current-clamp mode. Pipettes filled with K^+-based (for current-clamp) or Cs^+-based (for voltage-clamp) solution: 130 $KMeSO_4$/ $CsMeSO_4$, 2 $MgCl_2$, 10 diNaphosphocreatine, 10 HEPES, 4 ATP-Tris, 0.4 GTP-Tris and 0.3% biocytin (Sigma), pH 7.2–7.3, 280–290 mOsm/L. QX-314 was included in the intracellular solution in voltage-clamp recordings. Passive and active membrane properties were analyzed in current clamp mode. Passive membrane properties (resting membrane potential, input resistance, and membrane capacitance) were obtained during the first minute after membrane rupture. The cell firing was recorded by subjecting cells to multiple current step injections of varying amplitudes (20 to 200 pA). Voltage-clamp recordings were performed to analyze the excitatory and inhibitory drives received by VIP or O/A interneurons. For recordings of spontaneous excitatory postsynaptic currents (sEPSCs), the holding potential was fixed at –70 mV. Spontaneous inhibitory postsynaptic currents (sIPSCs) were recorded at 0 mV. Data acquisition (filtered at 2–3 kHz and digitized at 10kHz; Digidata 1440, Molecular Devices, CA, USA) was performed using the Multiclamp 700B amplifier and the Clampex 10.9 software (Molecular Devices). Series resistance (in voltage-clamp) or bridge balance (in current-clamp) were monitored throughout the experiment. Cells that had changes in series resistance or bridge balance (>15%), a resting membrane potential more positive than –45 mV or showed an increase in holding current (> –30 pA) during recording were discarded.

Electrophysiological data analysis

Analysis of electrophysiological recordings was performed using Clampfit 10.9 (Molecular Devices). For the analysis of the AP properties, the first AP appearing at the rheobase current pulse within a 50-ms time window was analysed. The AP threshold, amplitude, half-width, depolarization and repolarization rates, and the AP area were detected as previously described (Francavilla et al., 2020). The number of APs was assessed at the current pulse of +140–150 pA.

For the analysis of spontaneous synaptic currents, a minimum of 100 events (for EPSCs) and 200 events (for IPSCs) were sampled per cell over a 10 min period using an automated template search algorithm in Clampfit. All events were counted for frequency analysis.

Anatomical reconstruction and immunohistochemistry

For post hoc reconstruction, during whole-cell recordings neurons were filled with biocytin (Sigma). Slices containing the recorded cells were fixed overnight with 4% paraformaldehyde (PFA) at 4°C. To reveal biocytin, the slices were permeabilized with 0.3% Triton X-100 and incubated at 4°C with streptavidin conjugated Alexa-488 (1:1000) in Trizma-buffer (TB) overnight. Z-stacks of biocytin-filled cells were acquired with a 1-µm step using a 20x oil-immersion objective and Leica SP5 confocal microscope. Confocal stacks were merged for detailed reconstruction in Neurolucida 8.26.2 (MBF Bioscience). The I-S3 cells were identified based on the presence of axonal projections in the O/A (Acsády et al., 1996b; Tyan et al., 2014). The quantitative analysis of soma area and dendritic morphology was performed in Neurolucida (***Figure 2—Supplementary figure 3***). Sholl analysis was performed in radial coordinates, using a 50-µm step size with $r = 0$ centered on the cell soma.

All immunohistochemical tests were performed on free-floating hippocampal sections (50–70 µm thick) obtained with Leica VT1000S or PELCO EasySlicer vibratomes from mice perfused with 4% PFA. Sections were permeabilized with 0.25% Triton X-100 in PBS and incubated overnight at 4°C with primary antibodies followed by the secondary antibodies. The following primary antibodies were used in this study: goat anti-CR (1:1000; Santa Cruz, #sc-11644), chicken anti-GFP

(1:1000; Aves, #GFP-1020), mouse anti-β-amyloid, 1-16 (6E10) (1:3000; Covance, #SIG-39320), anti-human PHF-tau (1:1000; Thermo Scientific, #MN1020), mouse anti-VGAT (1:500; Synaptic Systems, #131011). Control immunohistochemical tests were performed by omitting the primary antibodies and incubating the sections in the mixture of secondary antibodies. Confocal images were acquired sequentially using a Leica TCS SP5 imaging system coupled with a 488-nm argon, a 543-nm HeNe and a 633-nm HeNe lasers. Cell counting was performed using stereological analysis within randomly selected regions of interest (500 x 700 µm) in the CA1 area. To sample the same hippocampal area along the septotemporal axis, only middle sections were analyzed. The cell counting was performed in 4–8 sections per animal from 3–4 different animals. For inhibitory axonal boutons density analysis, images of the CA1 O/A layer were acquired and the density of VGAT+ or VGAT+/CR+ boutons was measured using ImageJ (v1.53). VGAT+ puncta (0.5–0.8 µm) were counted automatically using the "Analyze particles" function with watershed segmentation within a 104 μm^2 area in the O/A in a single focal plan confocal image (2048 x 2048 pxl) at the same focal depth for all sections.

Stereotaxic injection and cannula implantation

Before stereotaxic surgery, nonTg or Tg mice were administered with buprenorphine slow release (0.1 mg/kg; i.p.) and lidocaine-bupivacaine (0.1 mL; local application at the site of incision). Mice were anesthetized with isoflurane and fixed in a stereotaxic frame (RWD). After incision, a hole was drilled in the skull over the site of injection in the right hemisphere. To express GCaMP6f in the CA1 region of the hippocampus, viral vectors were injected at the following coordinates: AP -2.2, ML -2, DV, -1.3 mm using a micro-pipette, which was attached to a microprocessor-controlled nanoliter injector (Nanoliter 2000; World Precision Instruments). AAV.mDlx.GCaMP6f (Addgene, #83899) was used to target inhibitory interneurons and AAV1-CamKII-GCaMP6f-WPRE (Penn Vector Core) was used to target primarily pyramidal neurons. The total volume of 100 nL was injected at the rate of 10 nL/sec. After injection, the pipette was kept at the site for

10 min and then withdrawn slowly to prevent backflow of the virus. For calcium imaging using wireless fiber photometry, the TeleFipho cannula (core 400 mm, NA 0.39, cladding 425 mm, ferrule 2.5 mm) was implanted at the same stereotaxic coordinates. Cannula was fixed to the skull with quick adhesive cement (C&B-Metabond), and the exposed skull was covered with dental cement mixed with carbon powder. Mice were injected with lactate ringer solution (0.1 mL/10 mg) and carprofen (0.1 mL/10 mg) post-surgery and for one day after surgery. Animal weight was monitored for 5 days post-surgery. Animals were allowed to recover for 2 weeks before the beginning of handling and calcium imaging experiments. After fiber photometry experiments, mice were perfused with 4% PFA and brain were sectioned (70 µm) on the next day. Sections containing the cannula track were mounted and confocal images were collected using the oil-immersion 20x (NA 0.8) objective and a laser-scanning Leica SP5 confocal microscope, and the expression of GCaMP6f as well as the cannula position were confirmed. Animals with imprecise cannula location were discarded from the analysis.

Wireless fiber photometry for in vivo calcium imaging

Calcium imaging was performed using the TeleFipho wireless fiber photometry device (Amuza Inc). The device calibration was done as previously described (Amalyan et al., 2022). Starting from two weeks post-injection of viral vectors, mice were exposed to daily handling for 4-5 days and habituated with a dummy head-stage attached to the implanted cannula for 2 days in their homecage before the start of behavioral studies. Following habituation, the TeleFipho head-stage was attached to the implanted cannula and mice were placed in their homecage or an arena where they were allowed to explore for 5 min. During this period, fiber photometry calcium signal was acquired wirelessly by the TeleFiR receiver (Amuza Inc.) at a sampling rate of 100 Hz. The calcium signal was quantified as the Z-score or ΔF/F, calculated in MATLAB with the following equations:

$$\text{Z-score} = \frac{(\mathrm{F}_{\mathrm{corrected}} - \mu)}{\sigma}$$

where Fcorrected is the de-trended signal, μ is the mean and σ is the standard deviation. The mean, maximum and area under the curve (AUC) of the Z-score

during a particular behavioral state was obtained using a MATLAB script detecting the dynamic threshold for calculation of Z-score.

$$\frac{\Delta F}{F} = \frac{(F_{corrected} - F_0)}{abs\,(F_0)}$$

where F0 is the minimum value in the Fcorrected trace.

The Z-scores were obtained using scripts written in MATLAB. The representative average traces of Z-scores for the period before, during and after the walk or exploration of D-zones or objects (***Figures 4 and 5***) were extracted using code written in MATLAB. First, to present the activity dynamics during walk/exploration bouts of variable durations using a representative curve, the event durations were normalized. Second, the time series of each event were converted to proportions i.e., each time point in the time series was divided by the total duration of the event. Hence the values on the x-axis can be considered as a fraction of the total event time where '0' and '1' means the start and end of the event, respectively. The object modulation variance (***Figure 5h***) was measured as the root mean square (RMS) of mean neuronal activity in the object zone.

Statistics

All statistical analysis was conducted in Sigma Plot 11.0, Clampfit 10.6 and Igor Pro. The data sets were first tested for normality with a Shapiro–Wilcoxon or Runs test. If data were normally distributed, standard parametric statistics were used: unpaired *t* tests for comparisons of two groups and two-way ANOVA for comparisons of multiple groups followed by Brown-Forsythe test. If data were not normally distributed, non-parametric Mann–Whitney or Wilcoxon rank tests were used for comparisons of two groups. The "p" values < 0.05 were considered significant.

For statistical analysis of electrophysiological recordings, we based our findings analyzing the data with linear mixed model (LMM), modelling animal as a random effect and genotype as fixed effect. We used this statistical analysis because we considered the number of mice as independent replicates and the number of cells in each mouse as repeated measures. LMM analysis was performed using IBM SPSS V29.0.0 software.

The data are presented using box plots and violon plots and show data distribution. Error bars represent the standard deviation, and the statistical results are presented as * = $p < 0.05$, ** = $p < 0.01$, *** = $p < 0.001$.

Figure Legends

Figure 1. VIP/CR I-S3 cells survive but accumulate intracellular Aβ and its precursors in VIP-Tg mice.

a. Confocal image of the CA1 hippocampal area showing intracellular accumulation of APP/Aβ (6E10) in cell bodies of the pyramidal layer in a 3-month-old VIP-Tg mouse (left, scale bar: 100 μm; inset shows the area indicated with a white box) and summary box plot showing the density of cells expressing APP/Aβ intracellularly in 3-month vs. 6-month-old mice (right; n = 8 slices from 3 animals per group). **b.** Summary bar graphs showing the average number of VIP+ cells expressing APP/Aβ intracellularly per slice (left), and representative confocal images of the VIP-IN labelled with eGFP and showing intracellular accumulation of APP/Aβ in a 6-month-old VIP-Tg mouse (right). Scale bar: 10 μm **c.** Representative confocal images of the CA1 hippocampal area in VIP-nonTg (top) and VIP-Tg (bottom) mice showing eGFP expression in VIP INs (left), CR expression (middle) and an overlay of both markers (right). Scale bar: 100 μm. **d.** Summary plots showing no changes in the number of VIP-INs (left; VIP-nonTg: n = 17 slices/3 animals; VIP-Tg: n = 13 slices/3 animals), CR-INs (middle; VIP-nonTg: n = 11 slices/3 animals; VIP-Tg: n = 11 slices/3 animals) and VIP/CR co-expressing I-S3 cells (right; VIP-nonTg: n = 11 slices/3 animals, VIP-Tg: n = 11 slices/3 animals) in VIP-Tg mice.

Figure 2. I-S3 cells exhibit wider spikes and lower firing rate in VIP-Tg mice.

a. Representative voltage responses (top, middle) showing the firing pattern of I-S3 cells in VIP-nonTg (left, black) and VIP-Tg (right, blue) mice in response to depolarizing and hyperpolarizing current injections (bottom). **b.** Representative voltage traces in VIP-nonTg (black) and VIP-Tg (blue) mice superimposed for the first (top) and last (bottom) AP showing the longer AP duration in VIP-Tg mice. **c.**

Summary plots showing the amplitude (left), half-width (middle left), depolarization rate (middle), repolarization rate (middle right) and area (right) of the first AP in I-S3 cells. *$p<0.05$ (VIP-nonTg: n = 8 cells/5 mice; VIP-Tg: n = 10 cells/3 mice). **d.** Summary plots showing changes in the AP amplitude (left), half-width (middle) and area (right) during the train of APs in I-S3 cells. ****$p<0.0001$ (VIP-nonTg: n = 7 cells/5 mice; VIP-Tg: n = 7 cells/3 mice). **e.** Summary plots showing no changes in the AP depolarization rate (left) but slower repolarization rate (right) during the train of APs in I-S3 cells. ****$p<0.0001$ (VIP-nonTg: n = 7 cells/5 mice; VIP-Tg: n = 7 cells/3 mice). **f.** Summary plot showing changes in the number of AP during the train of APs in relation to the injected current in I-S3 cells. The shaded areas show the SEM. *$p<0.05$ (VIP-nonTg: n = 7 cells/5 mice; VIP-Tg: n = 7 cells/3 mice).

Figure 3. Altered inhibition of CA1 interneurons in Tg mice.

a. Representative traces for sIPSCs in O/A INs from nonTg (top, black) and Tg (bottom, blue) mice. **b.** Summary plots showing the sIPSCs amplitude (left) and frequency (right) in nonTg (black) and Tg (blue) groups. Insets show data for animal-wise comparison. **$p<0.01$ (nonTg: n = 16 cells/5 mice; Tg: n = 10 cells/4 mice). **c.** Summary plots showing the sIPSC rise time left), decay time constant (middle), and charge transfer (right) in O/A INs of nonTg and Tg animals. *$p<0.05$, **$p<0.01$ (nonTg: n = 16 cells/5 mice; Tg: n = 10 cells/4 mice). **d.** Representative confocal images showing immunoreactivity for VGAT (left, scale bar: 20 μm) and VGAT+CR (right, scale bar: 5 μm) in the CA1 O/A of the nonTg (top) and Tg (bottom) mice. **e.** Summary plots showing no changes in the density of VGAT- and VGAT/CR-expressing axonal boutons in the O/A (nonTg: n = 19 slices/4 animals; Tg: n = 21 slices/4 animals).

Figure 4. Enhanced activation of CA1 interneurons during decision making and object exploration.

a. Schematic of cannula implantation and the experimental setup for wireless fiber photometry calcium imaging in freely behaving mice. **b.** Representative confocal

images of the CA1 hippocampal area showing the cannula track and GCaMPF6f expression in the CA1 parvalbumin-expressing (PV-INs) or somatostatin-expressing (SOM-INs), with a bar graph summarizing the fraction of PV-INs and SOM-INs contributing to the photometry signal. White arrowheads depict examples of cell bodies expressing GCaMPF6f. Scale bars: top, 100 μm; bottom, 50 μm. **c.** Summary plots showing the mean speed, mobility rate, total distance traveled (n = 13 animals per group) and the number of rearing episodes (nonTg: n = 9 animals; Tg: n = 7 animals) during the open field exploration in nonTg (black) and Tg (blue) animals. **d.** Representative individual (top) and average (bottom) traces obtained from O/A INs in nonTg (left, black) and Tg (right, blue) mice during walking in the open field arena. **e.** Summary plots showing the average (top) and peak (bottom) Z-scored values of calcium transients in O/A INs in nonTg (black) and Tg (blue) mice during walking (nonTg: n = 9 animals; Tg: n = 8 animals). **f.** Schematic of the behavioral paradigm for the T-maze: correct-choice animals visit an alternative to the previously visited arm during the 2nd trial. The decision zone (DZ) is illustrated with the shaded area. **g.** Bar graph showing the percentage of alternation in T-maze test in nonTg and Tg animals (nonTg: n = 9 animals; Tg: n = 6 animals). **h.** Summary plots showing the average (left) and peak (right) Z-scored values of calcium transients in O/A INs of nonTg (black) and Tg (blue) mice during exploration in the stem vs. DZ. Only mice making the correct choice (those that visited alternative to the previously visited arm) were included in this analysis. *$p<0.05$ (nonTg: n = 5 animals; Tg: n = 5 animals). **i.** Schematic of the arena used to examine the object-related modulation of neuronal activity (left), with summary plots showing the number of entries inside the object exploration zone (middle) and the average duration of object exploration episodes (right) (nonTg: n = 10 animals; Tg: n = 8 animals). **j.** Representative average traces (left) obtained from O/A INs in nonTg (black) and Tg (blue) mice during object exploration and summary plot of the average Z-scored values of calcium transients recorded in interneurons during object exploration periods. *$p<0.05$ (right, nonTg: n = 10 animals; Tg: n = 9 animals).

Figure 5. Altered activation of CA1 pyramidal cells during cognitive tasks. **a.** Representative confocal image of the CA1 hippocampal area showing the cannula track and GCaMPF6f expression in the CA1 PCs. Scale bar: 100 μm. **b.** Representative calcium traces and summary plots showing the peak amplitude (left) and frequency (right) of calcium transients recorded in the CA1 PCs in nonTg (black) and Tg (blue) mice when animals were in their homecage (nonTg: n = 4 animals; Tg: n = 5 animals). Insets show summary boxplots for animal-wise mean comparison. **c.** Representative average traces obtained from PCs in nonTg (black) and Tg (blue) mice during walking. The shaded areas show the SEM**. d.** Summary plots showing the peak and area under the curve (AUC) for Z-scored values of calcium transients in PCs of nonTg (black) and Tg (blue) mice during walking (nonTg: n = 4 animals; Tg: n = 5 animals). **e.** Representative average traces obtained from PCs in nonTg (black) and Tg (blue) mice during exploration in the D-zone of T-maze. The shaded areas show the SEM. **f.** Summary plots showing the average (left) and peak (right) Z-scored values of calcium transients in PCs of nonTg (black) and Tg (blue) mice during exploration in the stem vs. DZ. *$p<0.05$ (nonTg: n = 4 animals; Tg: n = 5 animals). **g.** Representative average traces obtained from PCs in nonTg (black) and Tg (blue) mice during object exploration. The shaded areas show the SEM. **h.** Summary plots showing the AUC (left) and the root mean square (RMS) for Z-scored values of calcium transients in PCs of nonTg (black) and Tg (blue) mice during object exploration. *$p<0.05$ (nonTg: n = 4 animals; Tg: n = 5 animals).

References

1. Acsády L, Arabadzisz D, Freund TF. 1996. Correlated morphological and neurochemical features identify different subsets of vasoactive intestinal polypeptide-immunoreactive interneurons in rat hippocampus. *Neuroscience* **73**:299–315. doi:10.1016/0306-4522(95)00610-9
2. Adler G, Brassen S, Jajcevic A. 2003. EEG coherence in Alzheimer's dementia. *J Neural Transm* **110**:1051–1058. doi:10.1007/s00702-003-0024-8
3. Algamal M, Russ AN, Miller MR, Hou SS, Maci M, Munting LP, Zhao Q, Gerashchenko D, Bacskai BJ, Kastanenka KV. 2022. Reduced excitatory neuron activity and interneuron-type-specific deficits in a mouse model of

Alzheimer's disease. *Commun Biol* **5**:1323. doi:10.1038/s42003-022-04268-x

4. Ali AB, Islam A, Constanti A. 2023. The fate of interneurons, GABA $_A$ receptor sub-types and perineuronal nets in Alzheimer's disease. *Brain Pathol* **33**:e13129. doi:10.1111/bpa.13129
5. Amalyan S, Tamboli S, Lazarevich I, Topolnik D, Bouman LH, Topolnik L. 2022. Enhanced motor cortex output and disinhibition in asymptomatic female mice with C9orf72 genetic expansion. *Cell Rep* **40**:111043. doi:10.1016/j.celrep.2022.111043
6. Arriaga M, Han EB. 2017. Dedicated Hippocampal Inhibitory Networks for Locomotion and Immobility. *J Neurosci* **37**:9222–9238. doi:10.1523/JNEUROSCI.1076-17.2017
7. Baglietto-Vargas D, Moreno-Gonzalez I, Sanchez-Varo R, Jimenez S, Trujillo-Estrada L, Sanchez-Mejias E, Torres M, Romero-Acebal M, Ruano D, Vizuete M, Vitorica J, Gutierrez A. 2010. Calretinin Interneurons are Early Targets of Extracellular Amyloid-β Pathology in PS1/AβPP Alzheimer Mice Hippocampus. *J Alzheimers Dis* **21**:119–132. doi:10.3233/JAD-2010-100066
8. Bezprozvanny I, Mattson MP. 2008. Neuronal calcium mishandling and the pathogenesis of Alzheimer's disease. *Trends Neurosci* **31**:454–463. doi:10.1016/j.tins.2008.06.005
9. Bilash OM, Chavlis S, Johnson CD, Poirazi P, Basu J. 2023. Lateral entorhinal cortex inputs modulate hippocampal dendritic excitability by recruiting a local disinhibitory microcircuit. *Cell Rep* **42**:111962. doi:10.1016/j.celrep.2022.111962
10. Brady DR, Mufson EJ. 1997. Parvalbumin-immunoreactive neurons in the hippocampal formation of Alzheimer's diseased brain. *Neuroscience* **80**:1113–1125. doi:10.1016/S0306-4522(97)00068-7
11. Busche MA, Chen X, Henning HA, Reichwald J, Staufenbiel M, Sakmann B, Konnerth A. 2012. Critical role of soluble amyloid-β for early hippocampal hyperactivity in a mouse model of Alzheimer's disease. *Proc Natl Acad Sci* **109**:8740–8745. doi:10.1073/pnas.1206171109
12. Busche MA, Eichhoff G, Adelsberger H, Abramowski D, Wiederhold K-H, Haass C, Staufenbiel M, Konnerth A, Garaschuk O. 2008. Clusters of Hyperactive Neurons Near Amyloid Plaques in a Mouse Model of Alzheimer's Disease. *Science* **321**:1686–1689. doi:10.1126/science.1162844
13. Busche MA, Konnerth A. 2016. Impairments of neural circuit function in Alzheimer's disease. *Philos Trans R Soc B Biol Sci* **371**:20150429. doi:10.1098/rstb.2015.0429
14. Caccavano A, Bozzelli PL, Forcelli PA, Pak DTS, Wu J-Y, Conant K, Vicini S. 2020. Inhibitory Parvalbumin Basket Cell Activity is Selectively Reduced during Hippocampal Sharp Wave Ripples in a Mouse Model of Familial Alzheimer's Disease. *J Neurosci* **40**:5116–5136. doi:10.1523/JNEUROSCI.0425-20.2020

15. Cattaud V, Bezzina C, Rey CC, Lejards C, Dahan L, Verret L. 2018. Early disruption of parvalbumin expression and perineuronal nets in the hippocampus of the Tg2576 mouse model of Alzheimer's disease can be rescued by enriched environment. *Neurobiol Aging* **72**:147–158. doi:10.1016/j.neurobiolaging.2018.08.024
16. Chakroborty S, Goussakov I, Miller MB, Stutzmann GE. 2009. Deviant ryanodine receptor-mediated calcium release resets synaptic homeostasis in presymptomatic 3xTg-AD mice. *J Neurosci* **29**:9458–9470. doi:10.1523/JNEUROSCI.2047-09.2009
17. Chatzikalymniou AP, Skinner FK. 2018. Deciphering the Contribution of Oriens-Lacunosum/Moleculare (OLM) Cells to Intrinsic θ Rhythms Using Biophysical Local Field Potential (LFP) Models. *eneuro* **5**:ENEURO.0146-18.2018. doi:10.1523/ENEURO.0146-18.2018
18. Chen L, Wick ZC, Vetere LM, Vaughan N, Jurkowski A, Galas A, Diego KS, Philipsberg P, Cai DJ, Shuman T. 2023. Progressive excitability changes in the medial entorhinal cortex in the 3xTg mouse model of Alzheimer's disease pathology. *J Neurosci.* 43: 7441-7454. doi: 10.1101/2023.05.30.542838.
19. Chung H, Park K, Jang HJ, Kohl MM, Kwag J. 2020. Dissociation of somatostatin and parvalbumin interneurons circuit dysfunctions underlying hippocampal theta and gamma oscillations impaired by amyloid β oligomers in vivo. *Brain Struct Funct* **225**:935–954. doi:10.1007/s00429-020-02044-3
20. Clark JK, Furgerson M, Crystal JD, Fechheimer M, Furukawa R, Wagner JJ. 2015. Alterations in synaptic plasticity coincide with deficits in spatial working memory in presymptomatic 3xTg-AD mice. *Neurobiol Learn Mem* **125**:152–162. doi:10.1016/j.nlm.2015.09.003
21. Cretin B, Sellal F, Philippi N, Bousiges O, Di Bitonto L, Martin-Hunyadi C, Blanc F. 2016. Epileptic Prodromal Alzheimer's Disease, a Retrospective Study of 13 New Cases: Expanding the Spectrum of Alzheimer's Disease to an Epileptic Variant? *J Alzheimers Dis* **52**:1125–1133. doi:10.3233/JAD-150096
22. Czigler B, Csikós D, Hidasi Z, Anna Gaál Z, Csibri É, Kiss É, Salacz P, Molnár M. 2008. Quantitative EEG in early Alzheimer's disease patients — Power spectrum and complexity features. *Int J Psychophysiol* **68**:75–80. doi:10.1016/j.ijpsycho.2007.11.002
23. David LS, Topolnik L. 2017. Target-specific alterations in the VIP inhibitory drive to hippocampal GABAergic cells after status epilepticus. *Exp Neurol* **292**:102–112. doi:10.1016/j.expneurol.2017.03.007
24. Davis KE, Easton A, Eacott MJ, Gigg J. 2013. Episodic-Like Memory for What-Where-Which Occasion is Selectively Impaired in the 3xTgAD Mouse Model of Alzheimer's Disease. *J Alzheimers Dis* **33**:681–698. doi:10.3233/JAD-2012-121543
25. Davis KE, Fox S, Gigg J. 2014. Increased Hippocampal Excitability in the 3xTgAD Mouse Model for Alzheimer's Disease *In Vivo*. *PLoS ONE* **9**: e91203. https://doi.org/10.1371/journal.pone.0091203

26. Drummond E, Wisniewski T. 2017. Alzheimer's disease: experimental models and reality. *Acta Neuropathol (Berl)* **133**:155–175. doi:10.1007/s00401-016-1662-x
27. Francavilla R, Guet-McCreight A, Amalyan S, Hui CW, Topolnik D, Michaud F, Marino B, Tremblay M-È, Skinner FK, Topolnik L. 2020. Alterations in Intrinsic and Synaptic Properties of Hippocampal CA1 VIP Interneurons During Aging. *Front Cell Neurosci* **14**:554405. doi:10.3389/fncel.2020.554405
28. Francavilla R, Luo X, Magnin E, Tyan L, Topolnik L. 2015. Coordination of dendritic inhibition through local disinhibitory circuits. *Front Synaptic Neurosci* **7**. doi:10.3389/fnsyn.2015.00005
29. Francavilla R, Villette V, Luo X, Chamberland S, Muñoz-Pino E, Camiré O, Wagner K, Kis V, Somogyi P, Topolnik L. 2018. Connectivity and network state-dependent recruitment of long-range VIP-GABAergic neurons in the mouse hippocampus. *Nat Commun* **9**:5043. doi:10.1038/s41467-018-07162-5
30. Francavilla R, Villette V, Martel O, Topolnik L. 2019. Calcium Dynamics in Dendrites of Hippocampal CA1 Interneurons in Awake Mice. *Front Cell Neurosci* **13**:98. doi:10.3389/fncel.2019.00098
31. Geiller T, Vancura B, Terada S, Troullinou E, Chavlis S, Tsagkatakis G, Tsakalides P, Ócsai K, Poirazi P, Rózsa BJ, Losonczy A. 2020. Large-Scale 3D Two-Photon Imaging of Molecularly Identified CA1 Interneuron Dynamics in Behaving Mice. *Neuron* **108**:968-983.e9. doi:10.1016/j.neuron.2020.09.013
32. Goutagny R, Gu N, Cavanagh C, Jackson J, Chabot J, Quirion R, Krantic S, Williams S. 2013. Alterations in hippocampal network oscillations and theta–gamma coupling arise before Aβ overproduction in a mouse model of Alzheimer's disease. *Eur J Neurosci* **37**:1896–1902. doi:10.1111/ejn.12233
33. Goutagny R, Krantic S. 2013. Hippocampal oscillatory activity in Alzheimer's disease: toward the identification of early biomarkers? *Aging Dis.* **4:**134-40.
34. Gu Z, Smith KG, Alexander GM, Guerreiro I, Dudek SM, Gutkin B, Jensen P, Yakel JL. 2020. Hippocampal Interneuronal α7 nAChRs Modulate Theta Oscillations in Freely Moving Mice. *Cell Rep* **31**:107740. doi:10.1016/j.celrep.2020.107740
35. Guet-McCreight A, Camiré O, Topolnik L, Skinner FK. 2016. Using a Semi-Automated Strategy to Develop Multi-Compartment Models That Predict Biophysical Properties of Interneuron-Specific 3 (IS3) Cells in Hippocampus. *eNeuro* **3**:ENEURO.0087-16.2016. doi:10.1523/ENEURO.0087-16.2016
36. Harris SS, Wolf F, De Strooper B, Busche MA. 2020. Tipping the Scales: Peptide-Dependent Dysregulation of Neural Circuit Dynamics in Alzheimer's Disease. *Neuron* **107**:417–435. doi:10.1016/j.neuron.2020.06.005

37. Hernandez-Frausto M, Bilash O, Masurkar A, Basu J. 2023 Local and long-range GABAergic circuits in hippocampal area CA1 and their link to Alzheimer's disease. *Front. Neural Circuit* **17**: https://doi.org/10.3389/fncir.2023.1223891
38. Herrmann C, Demiralp T. 2005. Human EEG gamma oscillations in neuropsychiatric disorders. *Clin Neurophysiol* **116**:2719–2733. doi:10.1016/j.clinph.2005.07.007
39. Hijazi S, Heistek TS, Scheltens P, Neumann U, Shimshek DR, Mansvelder HD, Smit AB, Van Kesteren RE. 2020. Early restoration of parvalbumin interneuron activity prevents memory loss and network hyperexcitability in a mouse model of Alzheimer's disease. *Mol Psychiatry* **25**:3380–3398. doi:10.1038/s41380-019-0483-4
40. Hof PR, Nimchinsky EA, Celio MR, Bouras C, Morrison JH. 1993. Calretinin-immunoreactive neocortical interneurons are unaffected in Alzheimer's disease. *Neurosci Lett* **152**:145–149. doi:10.1016/0304-3940(93)90504-E
41. Inayat S, McAllister BB, Whishaw IQ, Mohajerani MH. 2023. Hippocampal conjunctive and complementary CA1 populations relate sensory events to movement. *iScience*. **26:**106481. doi: 10.1016/j.isci.2023.106481.
42. Javonillo DI, Tran KM, Phan J, Hingco E, Kramár EA, Da Cunha C, Forner S, Kawauchi S, Milinkeviciute G, Gomez-Arboledas A, Neumann J, Banh CE, Huynh M, Matheos DP, Rezaie N, Alcantara JA, Mortazavi A, Wood MA, Tenner AJ, MacGregor GR, Green KN, LaFerla FM. 2022. Systematic Phenotyping and Characterization of the 3xTg-AD Mouse Model of Alzheimer's Disease. *Front Neurosci* **15**:785276. doi:10.3389/fnins.2021.785276
43. Jones EA, Gillespie AK, Yoon SY, Frank LM, Huang Y. 2019. Early Hippocampal Sharp-Wave Ripple Deficits Predict Later Learning and Memory Impairments in an Alzheimer's Disease Mouse Model. *Cell Rep* **29**:2123-2133.e4. doi:10.1016/j.celrep.2019.10.056
44. Kullander K, Topolnik L. 2021. Cortical disinhibitory circuits: cell types, connectivity and function. *Trends Neurosci* **44**:643–657. doi:10.1016/j.tins.2021.04.009
45. LaFerla FM, Green KN, Oddo S. 2007. Intracellular amyloid-β in Alzheimer's disease. *Nature Reviews Neuroscience* **8**:499-509. doi:10.1038/nrn2168
46. Lauritzen I, Pardossi-Piquard R, Bauer C, Brigham E, Abraham J.-D, Ranaldi S, Fraser P, St-George-Hyslop P, Le Thuc O, Espin V, Chami L, Dunys J, Checler F. 2012. The β-secretase-derived C-terminal fragment of βAPP, C99, but not Aβ, is a key contributor to early intraneuronal lesions in triple-transgenic mouse hippocampus. *The Journal of neuroscience : the official journal of the Society for Neuroscience* **32**:16243-1655a. doi:10.1523/JNEUROSCI.2775-12.2012
47. Li S, Hong S, Shepardson NE, Walsh DM, Shankar GM, Selkoe D. 2009. Soluble oligomers of amyloid β-protein facilitate hippocampal long-term

depression by disrupting neuronal glutamate uptake. *Neuron* **62**:788-801. doi:10.1016/j.neuron.2009.05.012

48. Lovett-Barron M, Turi GF, Kaifosh P, Lee PH, Bolze F, Sun X-H, Nicoud J-F, Zemelman BV, Sternson SM, Losonczy A. 2012. Regulation of neuronal input transformations by tunable dendritic inhibition. *Nat Neurosci* **15**:423–430. doi:10.1038/nn.3024
49. Luo X, Guet-McCreight A, Villette V, Francavilla R, Marino B, Chamberland S, Skinner FK, Topolnik L. 2020. Synaptic Mechanisms Underlying the Network State-Dependent Recruitment of VIP-Expressing Interneurons in the CA1 Hippocampus. *Cereb Cortex* **30**:3667–3685. doi:10.1093/cercor/bhz334
50. Luo X, Muñoz-Pino E, Francavilla R, Vallée M, Droit A, Topolnik L. 2019. Transcriptomic profile of the subiculum-projecting VIP GABAergic neurons in the mouse CA1 hippocampus. *Brain Struct Funct* **224**:2269–2280. doi:10.1007/s00429-019-01883-z
51. Mably AJ, Gereke BJ, Jones DT, Colgin LL. 2017. Impairments in spatial representations and rhythmic coordination of place cells in the 3xTg mouse model of Alzheimer's disease. *Hippocampus* **27**:378–392. doi:10.1002/hipo.22697
52. Magnin E, Francavilla R, Amalyan S, Gervais E, David LS, Luo X, Topolnik L. 2019. Input-Specific Synaptic Location and Function of the α5 GABA $_A$ Receptor Subunit in the Mouse CA1 Hippocampal Neurons. *J Neurosci* **39**:788–801. doi:10.1523/JNEUROSCI.0567-18.2018
53. Manville, RW, Abbott GW. 2021. The Amyloid Precursor Protein C99 Fragment Modulates Voltage-Gated Potassium Channels. *Cellular Physiology and Biochemistry : International Journal of Experimental Cellular Physiology, Biochemistry, and Pharmacology* **55**:157–70. doi: 10.33594/000000397.
54. Martinez-Losa M, Tracy TE, Ma K, Verret L, Clemente-Perez A, Khan AS, Cobos I, Ho K, Gan L, Mucke L, Alvarez-Dolado M, Palop JJ. 2018. Nav1.1-Overexpressing Interneuron Transplants Restore Brain Rhythms and Cognition in a Mouse Model of Alzheimer's Disease. *Neuron* **98**:75-89.e5. doi:10.1016/j.neuron.2018.02.029
55. Mastrangelo MA, Bowers WJ. 2008. Detailed immunohistochemical characterization of temporal and spatial progression of Alzheimer's disease-related pathologies in male triple-transgenic mice. *BMC Neurosci* **9**:81. doi:10.1186/1471-2202-9-81
56. Mikkonen M, Alafuzoff I, Tapiola T, Soininen H, Miettinen R. 1999. Subfield- and layer-specific changes in parvalbumin, calretinin and calbindin-D28k immunoreactivity in the entorhinal cortex in Alzheimer's disease. *Neuroscience* **92**:515–532. doi:10.1016/S0306-4522(99)00047-0
57. Mikulovic S, Restrepo CE, Siwani S, Bauer P, Pupe S, Tort ABL, Kullander K, Leão RN. 2018. Ventral hippocampal OLM cells control type 2 theta oscillations and response to predator odor. *Nat Commun* **9**:3638. doi:10.1038/s41467-018-05907-w

58. Mondragón-Rodríguez S, Gu N, Manseau F, Williams S. 2018. Alzheimer's Transgenic Model Is Characterized by Very Early Brain Network Alterations and β-CTF Fragment Accumulation: Reversal by β-Secretase Inhibition. *Frontiers in cellular neuroscience* **12**:121. doi:10.3389/fncel.2018.00121
59. Montinaro C, Pisanello M, Bianco M, Spagnolo B, Pisano F, Balena A, De Nuccio F, Lofrumento DD, Verri T, De Vittorio M, Pisanello F. 2021. Influence of the anatomical features of different brain regions on the spatial localization of fiber photometry signals. *Biomed Opt Express* **12**:6081. doi:10.1364/BOE.439848
60. Moretti DV, Pievani M, Geroldi C, Binetti G, Zanetti O, Rossini PM, Frisoni GB. 2010. EEG Markers Discriminate Among Different Subgroup of Patients With Mild Cognitive Impairment. *Am J Alzheimers Dis Dementiasr* **25**:58–73. doi:10.1177/1533317508329814
61. Myers A, McGonigle P. 2019. Overview of Transgenic Mouse Models for Alzheimer's Disease. *Curr Protoc Neurosci* **89**:e81. doi:10.1002/cpns.81
62. Noristani HN, Meadows RS, Olabarria M, Verkhratsky A, Rodríguez JJ. 2011. Increased hippocampal CA1 density of serotonergic terminals in a triple transgenic mouse model of Alzheimer's disease: an ultrastructural study. *Cell Death Dis* **2**:e210–e210. doi:10.1038/cddis.2011.79
63. Oddo S, Caccamo A, Shepherd JD, Murphy MP, Golde TE, Kayed R, Metherate R, Mattson MP, Akbari Y, LaFerla FM. 2003. Triple-Transgenic Model of Alzheimer's Disease with Plaques and Tangles. *Neuron* **39**:409–421. doi:10.1016/S0896-6273(03)00434-3
64. Olah VJ, Goettemoeller AM, Rayaprolu S, Dammer EB, Seyfried NT, Rangaraju S, Dimidschstein J, Rowan MJ. 2022. Biophysical Kv3 channel alterations dampen excitability of cortical PV interneurons and contribute to network hyperexcitability in early Alzheimer's. *eLife* **11**:e75316. doi:10.7554/eLife.75316
65. Pairojana T, Phasuk S, Suresh P, Huang S-P, Pakaprot N, Chompoopong S, Hsieh T-C, Liu IY. 2021. Age and gender differences for the behavioral phenotypes of 3xTg alzheimer's disease mice. *Brain Res* **1762**:147437. doi:10.1016/j.brainres.2021.147437
66. Palop JJ, Mucke L. 2016. Network abnormalities and interneuron dysfunction in Alzheimer disease. *Nat Rev Neurosci* **17**:777–792. doi:10.1038/nrn.2016.141
67. Palop JJ, Mucke L. 2009. Epilepsy and Cognitive Impairments in Alzheimer Disease. *Arch Neurol* **66**:435. doi:10.1001/archneurol.2009.15
68. Pisano F, Pisanello M, Lee SJ, Lee J, Maglie E, Balena A, Sileo L, Spagnolo B, Bianco M, Hyun M, De Vittorio M, Sabatini BL, Pisanello F. 2019. Depth-resolved fiber photometry with a single tapered optical fiber implant. *Nat Methods* **16**:1185–1192. doi:10.1038/s41592-019-0581-x
69. Rice HC, Marcassa G, Chrysidou I, Horré K, Young-Pearse TL, Müller UC, Saito T, Saido TC, Vassar R, de Wit J, De Strooper B. 2020. Contribution of GABAergic interneurons to amyloid-β plaque pathology in an APP

knock-in mouse model. *Mol Neurodegener* **15**:3. doi:10.1186/s13024-019-0356-y

70. Rodriguez A, Zhang H, Klaminder J, Brodin T, Andersson PL, Andersson M. 2018. *ToxTrac* : A fast and robust software for tracking organisms. *Methods Ecol Evol* **9**:460–464. doi:10.1111/2041-210X.12874
71. Royer S, Zemelman BV, Losonczy A, Kim J, Chance F, Magee JC, Buzsáki G. 2012. Control of timing, rate and bursts of hippocampal place cells by dendritic and somatic inhibition. *Nat Neurosci* **15**:769–775. doi:10.1038/nn.3077
72. Schmid LC, Mittag M, Poll S, Steffen J, Wagner J, Geis H-R, Schwarz I, Schmidt B, Schwarz MK, Remy S, Fuhrmann M. 2016. Dysfunction of Somatostatin-Positive Interneurons Associated with Memory Deficits in an Alzheimer's Disease Model. *Neuron* **92**:114–125. doi:10.1016/j.neuron.2016.08.034
73. Schneider F, Baldauf K, Wetzel W, Reymann KG. 2014. Behavioral and EEG changes in male 5xFAD mice. *Physiol Behav* **135**:25–33. doi:10.1016/j.physbeh.2014.05.041
74. Scott L, Feng J, Kiss T, Needle E, Atchison K, Kawabe TT, Milici AJ, Hajós-Korcsok É, Riddell D, Hajós M. 2012. Age-dependent disruption in hippocampal theta oscillation in amyloid-β overproducing transgenic mice. *Neurobiol Aging* **33**:1481.e13-1481.e23. doi:10.1016/j.neurobiolaging.2011.12.010
75. Shi A, Petrache AL, Shi J, Ali AB. 2020. Preserved Calretinin Interneurons in an App Model of Alzheimer's Disease Disrupt Hippocampal Inhibition via Upregulated P2Y1 Purinoreceptors. *Cereb Cortex* **30**:1272–1290. doi:10.1093/cercor/bhz165
76. Soltesz I, Losonczy A. 2018. CA1 pyramidal cell diversity enabling parallel information processing in the hippocampus. *Nat Neurosci* **21**:484–493. doi:10.1038/s41593-018-0118-0
77. Stimmell AC, Baglietto-Vargas D, Moseley SC, Lapointe V, Thompson LM, LaFerla FM, McNaughton BL, Wilber AA. 2019. Impaired Spatial Reorientation in the 3xTg-AD Mouse Model of Alzheimer's Disease. *Sci Rep* **9**:1311. doi:10.1038/s41598-018-37151-z
78. Takasugi N, Komai M, Kaneshiro N, Ikeda A, Kamikubo Y, Uehara T. 2023. The Pursuit of the "Inside" of the Amyloid Hypothesis-Is C99 a Promising Therapeutic Target for Alzheimer's Disease? *Cells* **12**(3). doi:10.3390/cells12030454
79. Tamboli S, Singh S, Topolnik D, Barkat M, Guett-McCreight A, Topolnik L. 2024. Hippocampal CA1 VIP interneurons detect novelty in the environment and regulate recognition memory. *Cell Reports 43:114115 https://doi.org/10.1016/j.celrep.2024.114115*
80. Topolnik L, Tamboli S. 2022. The role of inhibitory circuits in hippocampal memory processing. *Nat Rev Neurosci* **23**:476–492. doi:10.1038/s41583-022-00599-0
81. Turi GF, Li W-K, Chavlis S, Pandi I, O'Hare J, Priestley JB, Grosmark AD, Liao Z, Ladow M, Zhang JF, Zemelman BV, Poirazi P, Losonczy A. 2019.

Vasoactive Intestinal Polypeptide-Expressing Interneurons in the Hippocampus Support Goal-Oriented Spatial Learning. *Neuron* **101**:1150-1165.e8. doi:10.1016/j.neuron.2019.01.009

82. Tyan L, Chamberland S, Magnin E, Camiré O, Francavilla R, David LS, Deisseroth K, Topolnik L. 2014. Dendritic Inhibition Provided by Interneuron-Specific Cells Controls the Firing Rate and Timing of the Hippocampal Feedback Inhibitory Circuitry. *J Neurosci* **34**:4534–4547. doi:10.1523/JNEUROSCI.3813-13.2014
83. Van Der Hiele K, Vein AA, Van Der Welle A, Van Der Grond J, Westendorp RGJ, Bollen ELEM, Van Buchem MA, Van Dijk JG, Middelkoop HAM. 2007. EEG and MRI correlates of mild cognitive impairment and Alzheimer's disease. *Neurobiol Aging* **28**:1322–1329. doi:10.1016/j.neurobiolaging.2006.06.006
84. Verret L, Mann EO, Hang GB, Barth AMI, Cobos I, Ho K, Devidze N, Masliah E, Kreitzer AC, Mody I, Mucke L, Palop JJ. 2012. Inhibitory Interneuron Deficit Links Altered Network Activity and Cognitive Dysfunction in Alzheimer Model. *Cell* **149**:708–721. doi:10.1016/j.cell.2012.02.046
85. Vitale P, Salgueiro-Pereira AR, Lupascu CA, Willem M, Migliore R, Migliore M, Marie H. 2021. Analysis of Age-Dependent Alterations in Excitability Properties of CA1 Pyramidal Neurons in an APPPS1 Model of Alzheimer's Disease. *Front Aging Neurosci* **13**:668948. doi:10.3389/fnagi.2021.668948
86. Waller R, Mandeya M, Viney E, Simpson JE, Wharton SB. 2020. Histological characterization of interneurons in Alzheimer's disease reveals a loss of somatostatin interneurons in the temporal cortex. *Neuropathology* **40**:336–346. doi:10.1111/neup.12649

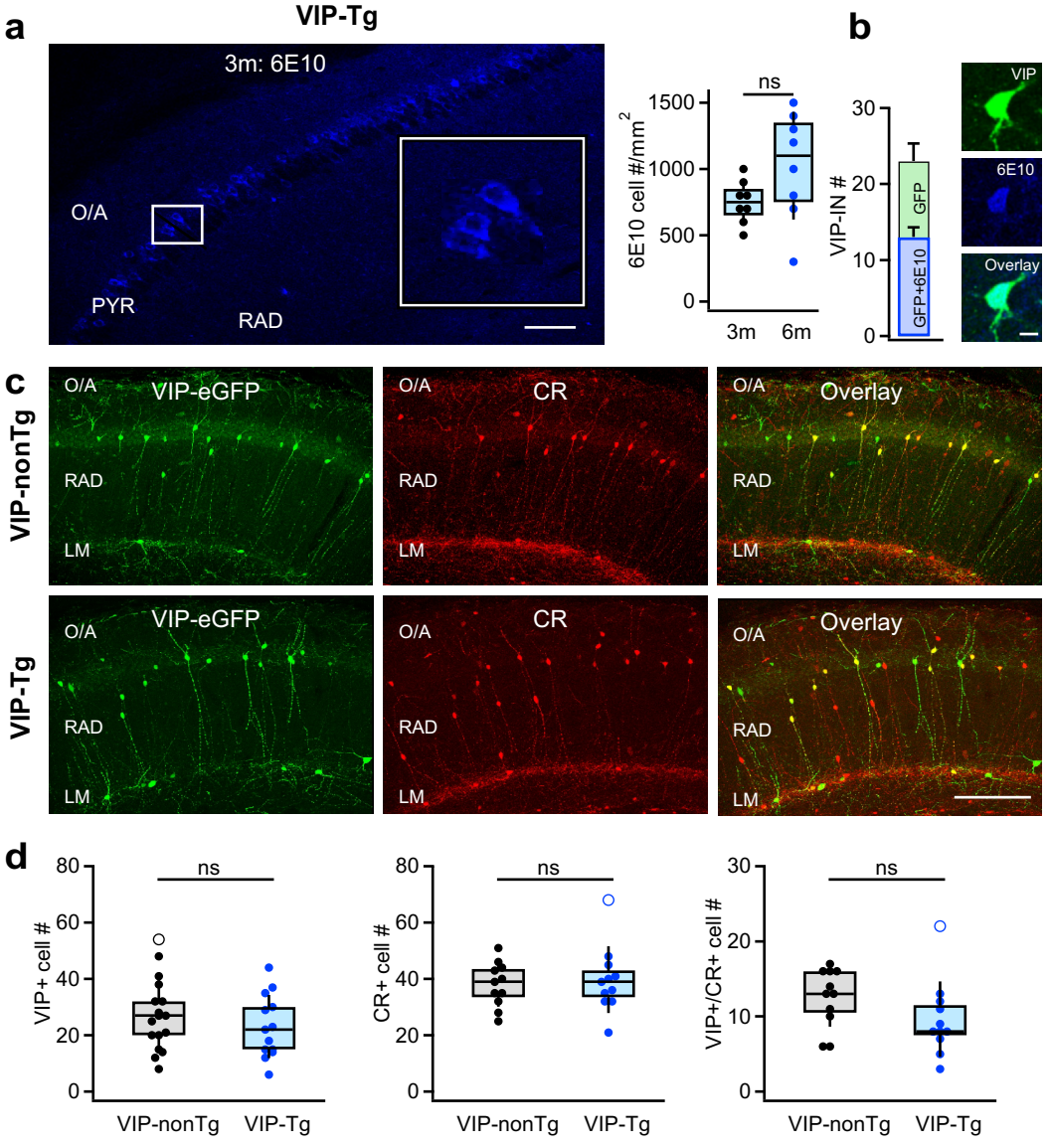
a
VIP-Tg
3m: 6E10
O/A
PYR
RAD
b
ns
6E10 cell #/mm2
1500
1000
500
0
3m
6m
VIP-IN #
30
20
10
0
GFP
GFP+6E10
VIP
6E10
Overlay
c
VIP-nonTg
VIP-Tg
O/A
VIP-eGFP
CR
Overlay
RAD
LM
d
VIP+ cell #
CR+ cell #
VIP+/CR+ cell #
ns
VIP-nonTg
VIP-Tg

Figure 1.

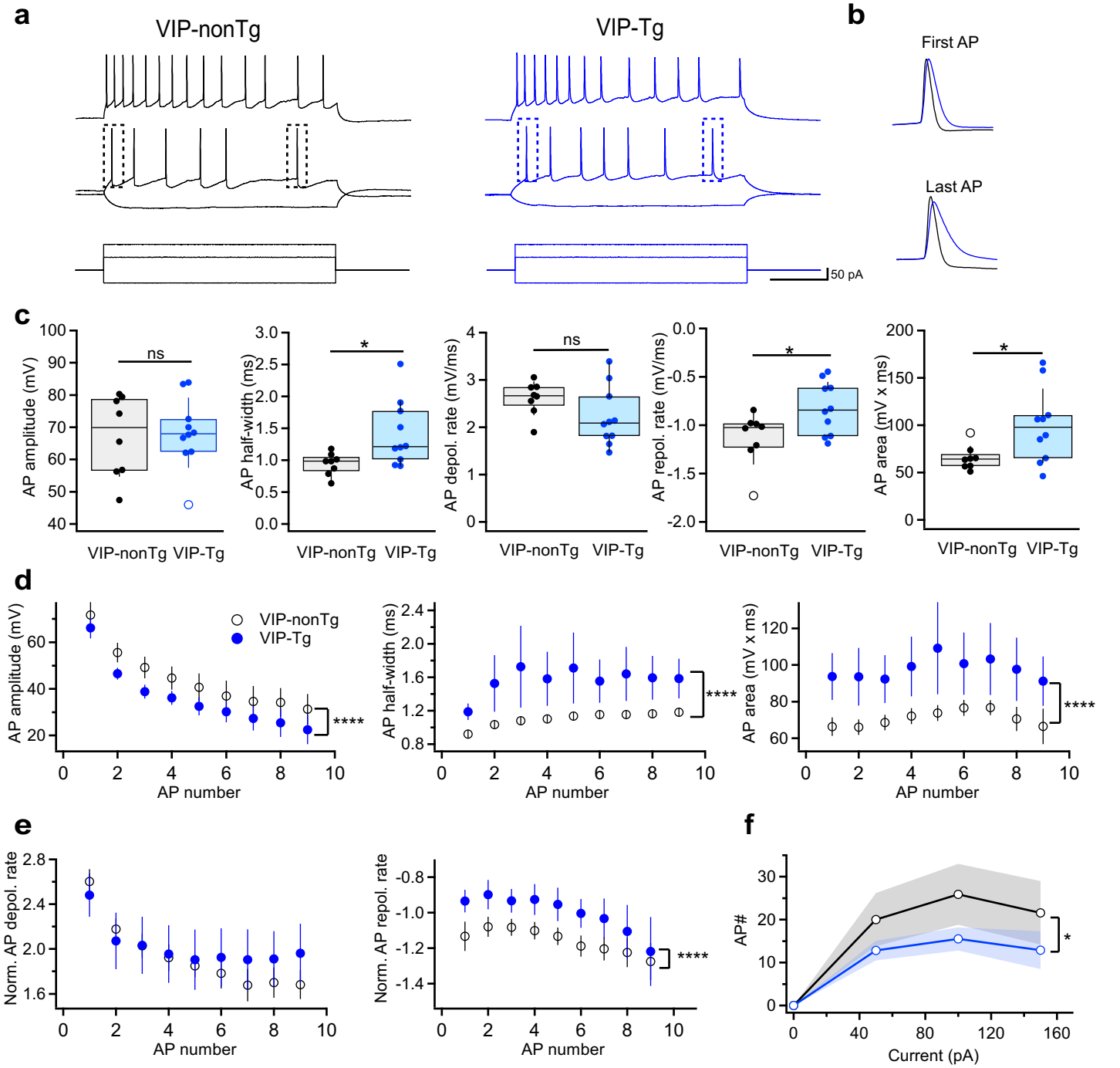
a
VIP-nonTg
VIP-Tg
50 pA
b
First AP
Last AP
c
AP amplitude (mV)
ns
AP half-width (ms)
*
AP depol. rate (mV/ms)
ns
AP repol. rate (mV/ms)
*
AP area (mV x ms)
*
VIP-nonTg
VIP-Tg
d
AP amplitude (mV)
VIP-nonTg
VIP-Tg
****
AP half-width (ms)
****
AP area (mV x ms)
****
AP number
e
Norm. AP depol. rate
Norm. AP repol. rate
****
AP number
f
AP#
*
Current (pA)

Figure 2.

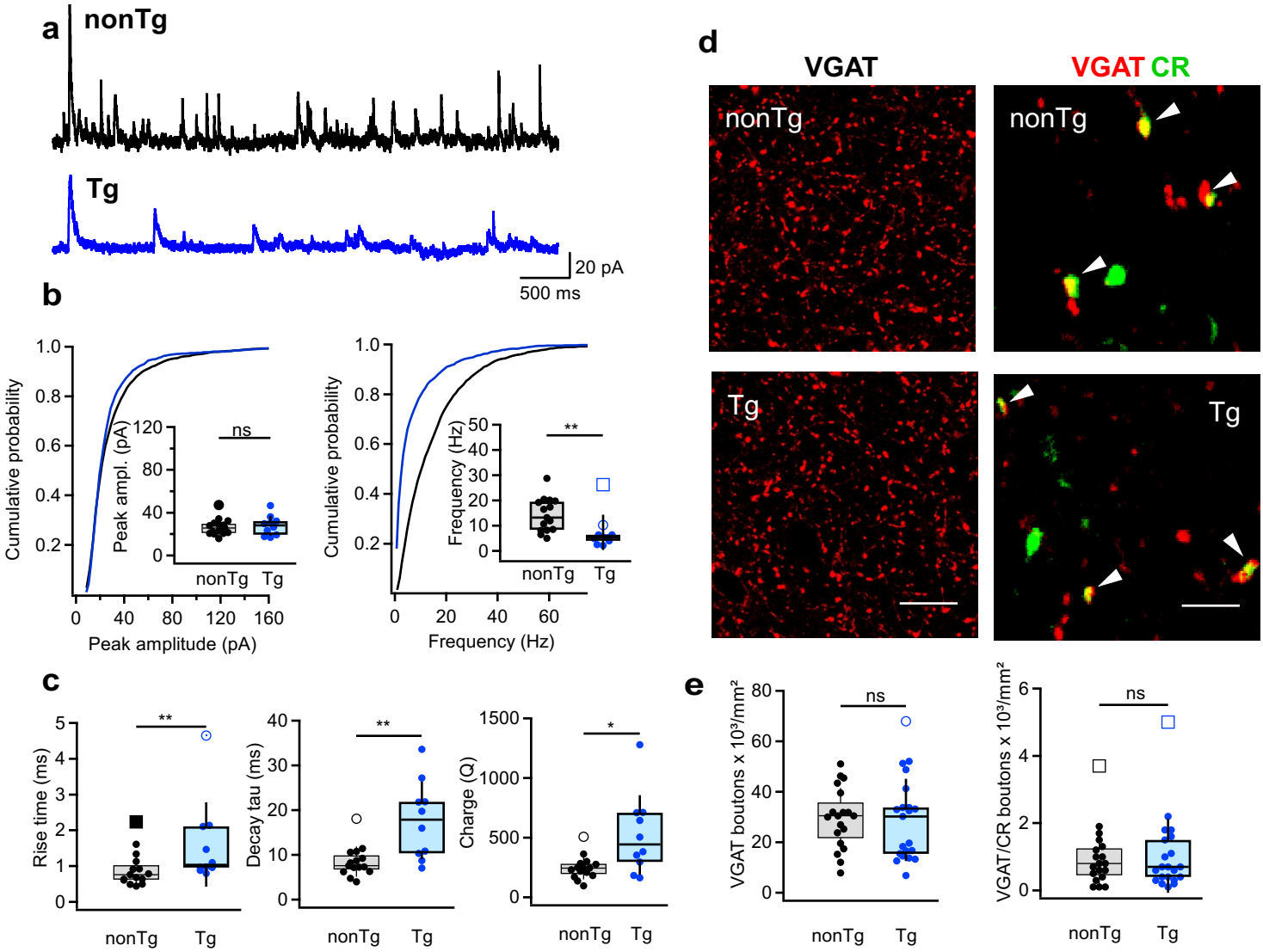
a
nonTg
Tg
20 pA
500 ms
b
Cumulative probability
Peak ampl. (pA)
ns
nonTg
Tg
Peak amplitude (pA)
Frequency (Hz)
**
c
Rise time (ms)
Decay tau (ms)
Charge (Q)
d
VGAT
VGAT CR
e
VGAT boutons x 10³/mm²
VGAT/CR boutons x 10³/mm²

Figure 3.

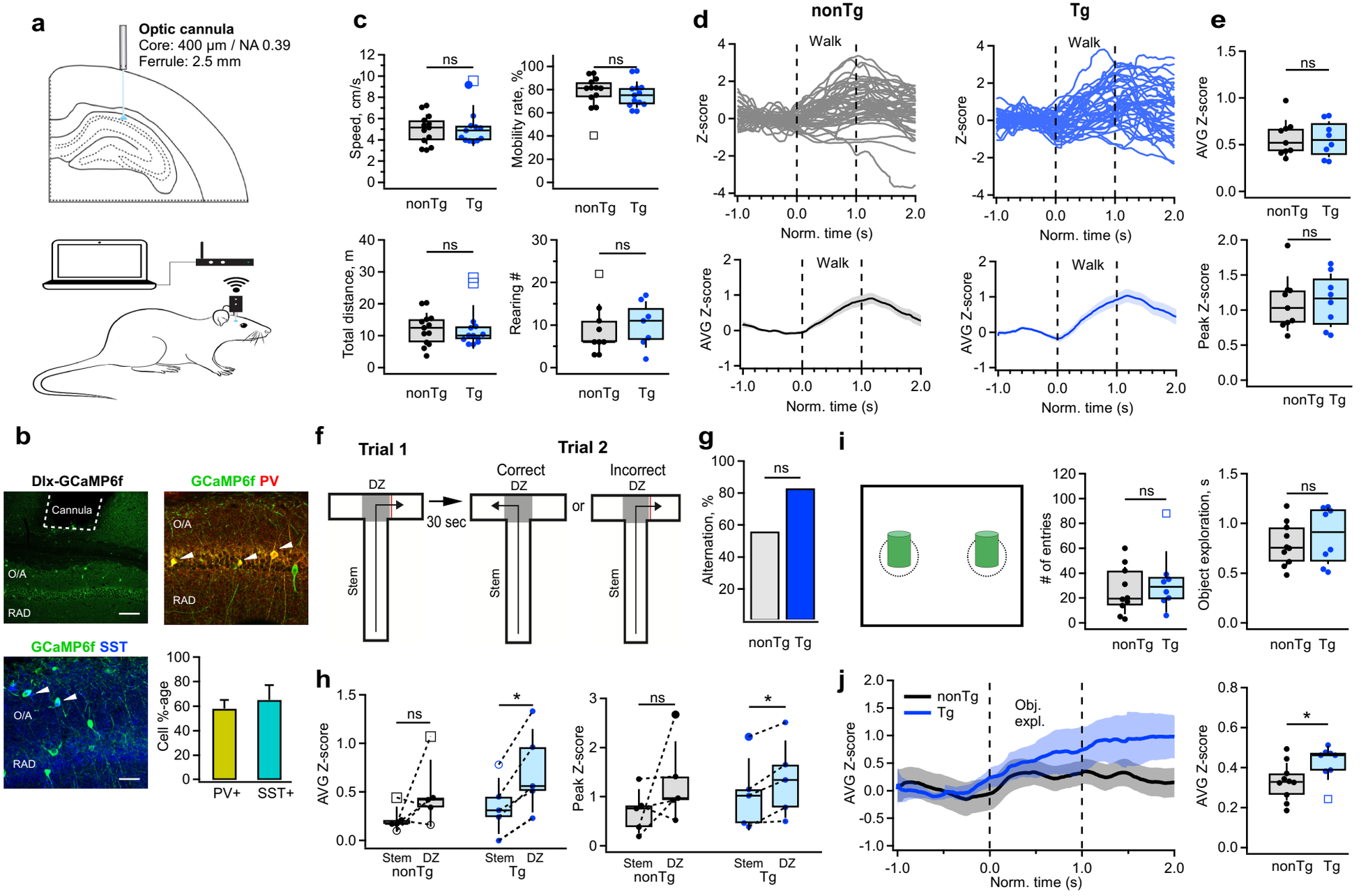
a
Optic cannula
Core: 400 µm / NA 0.39
Ferrule: 2.5 mm
b
Dlx-GCaMP6f
Cannula
O/A
RAD
GCaMP6f PV
GCaMP6f SST
Cell %-age
PV+
SST+
c
Speed, cm/s
Mobility rate, %
Total distance, m
Rearing #
ns
nonTg
Tg
d
nonTg
Tg
Walk
Z-score
AVG Z-score
Norm. time (s)
e
AVG Z-score
Peak Z-score
f
Trial 1
Trial 2
Correct
Incorrect
DZ
Stem
30 sec
or
g
Alternation, %
h
AVG Z-score
Peak Z-score
Stem
DZ
i
# of entries
Object exploration, s
j
Obj. expl.

Figure 4.

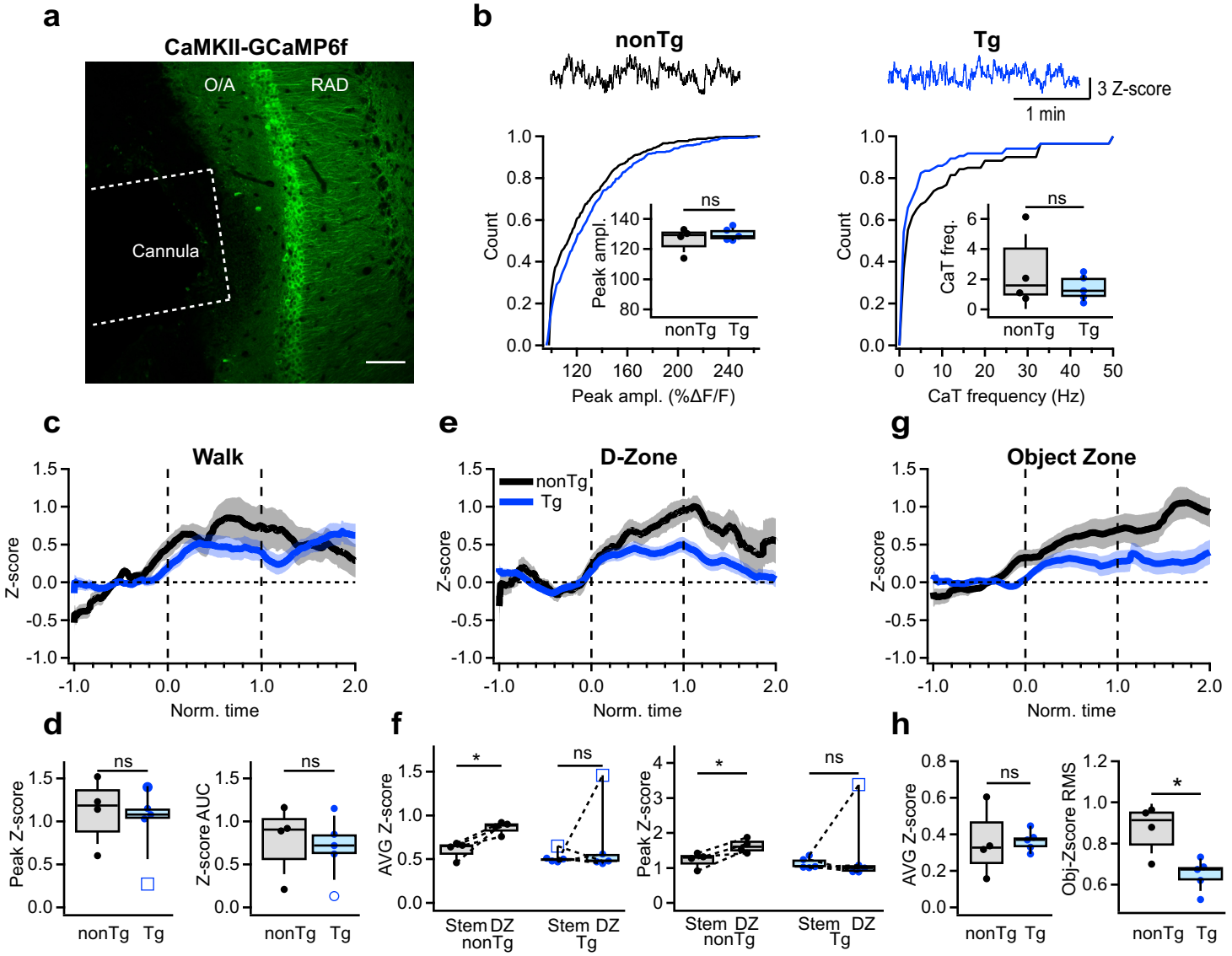
a
CaMKII-GCaMP6f
O/A
RAD
Cannula
b
nonTg
Tg
3 Z-score
1 min
Count
Peak ampl. (%ΔF/F)
Peak ampl.
ns
nonTg
Tg
CaT frequency (Hz)
CaT freq.
c
Walk
Z-score
Norm. time
e
D-Zone
nonTg
Tg
g
Object Zone
d
Peak Z-score
Z-score AUC
f
AVG Z-score
Stem DZ
nonTg
Stem DZ
Tg
*
h
Obj-Zscore RMS

Figure 5.

Supplementary Table 1. Summary of statistical analysis conducted throughout the study.

Notes:

1) *The reported n corresponds to the number of animals, cells (underlined) or slices (italic).*
2) *Animals of both sexes with equal distribution were used throughout the study.*

Figure	Condition	n	Test	*P* value
Fig 1a	6E10+ cell density: 3-month vs. 6-month	3,*8* vs. 3,*8*	Wilcoxon Rank	0.1027
Fig 1d	VIP+ cell density: VIP-nonTg vs. VIP-Tg	3,*17* vs. 3,*13*	Wilcoxon Rank	0.4442
	CR+ cell density: VIP-nonTg vs. VIP-Tg	3,*11* vs. 3,*11*	Wilcoxon Rank	0.8720
	VIP+/CR+ cell density: VIP-nonTg vs. VIP-Tg	3,*11* vs. 3,*11*	Wilcoxon Rank	0.0751
Fig 2c	AP amplitude: VIP-nonTg vs. VIP-Tg	5,8 vs. 3,10	LMM	0.843
	AP half-width: VIP-nonTg vs. VIP-Tg	5,8 vs. 3,10	LMM	0.018*
	AP depolarization rate: VIP-nonTg vs. VIP-Tg	5,8 vs. 3,10	LMM	0.461
	AP repolarization rate: VIP-nonTg vs. VIP-Tg	5,8 vs. 3,10	LMM	0.024*
	AP area: VIP-nonTg vs. VIP-Tg	5,8 vs. 3,10	LMM	0.025*
Fig 2d	AP amplitude: VIP-nonTg vs. VIP-Tg	5,7 vs. 3,7	Two-way ANOVA	<0.0001****
	AP half-width: VIP-nonTg vs. VIP-Tg	5,7 vs. 3,7	Two-way ANOVA	<0.0001****
	AP area: VIP-nonTg vs. VIP-Tg	5,7 vs. 3,7	Two-way ANOVA	<0.0001****
Fig 2e	Norm. AP depol. rate: VIP-nonTg vs. VIP-Tg	5,7 vs. 3,7	Two-way ANOVA	0.9998
	Norm. AP repol. rate: VIP-nonTg vs. VIP-Tg	5,7 vs. 3,7	Two-way ANOVA	<0.0001****
Fig 2f	AP number: VIP-nonTg vs. VIP-Tg	5,7 vs. 3,7	Two-way ANOVA	0.0264*
Fig 3b	sIPSC amplitude: nonTg vs. Tg	5, 16 vs. 4, 10	Wilcoxon Rank	1.0000
	sIPSC frequency: nonTg vs. Tg	5, 16 vs. 4, 10	Wilcoxon Rank	0.0017**
Fig 3c	sIPSC rise time: nonTg vs. Tg	5, 16 vs. 4, 10	Wilcoxon Rank	0.0095**
	sIPSC decay tau: nonTg vs. Tg	5, 16 vs. 4, 10	Wilcoxon Rank	0.0017**
	sIPSC charge transfer: nonTg vs. Tg	5, 16 vs. 4, 10	Wilcoxon Rank	0.0214*
Fig 3e	VGAT bouton density: nonTg vs. Tg	4,*19* vs. 4,*21*	Unpaired t-test	0.8886
	VGAT/CR bouton density: nonTg vs. Tg	4,*19* vs. 4,*21*	Wilcoxon Rank	0.9039
Fig 4c	Animal speed: nonTg vs. Tg	13/group	Wilcoxon Rank	0.9398
	Animal mobility rate: nonTg vs. Tg	13/group	Wilcoxon Rank	0.4637
	Total distance: nonTg vs. Tg	13/group	Wilcoxon Rank	0.7432
	Rearing: nonTg vs. Tg	9 vs. 7	Wilcoxon Rank	0.4990
Fig 4e	Walk AVG Z-score: nonTg vs. Tg	9 vs. 8	Wilcoxon Rank	0.9254
	Walk Peak Z-score: nonTg vs. Tg	9 vs. 8	Wilcoxon Rank	0.6732
Fig 4g	Alternation-%: nonTg vs. Tg	9 vs. 6	Fisher's Exact	0.2517
Fig 4h	nonTg AVG Z-score stem vs. D-zone	5	Wilcoxon Signed	0.3125
	Tg AVG Z-score stem vs. D-zone	5	Wilcoxon Signed	0.0313*
	nonTg Peak Z-score stem vs. D-zone	5	Wilcoxon Signed	0.625
	Tg Peak Z-score stem vs. D-zone	5	Wilcoxon Signed	0.0313*
Fig 4i	Object entries: nonTg vs. Tg	10 vs. 8	Wilcoxon Rank	0.7700
	Object time: nonTg vs. Tg	10 vs. 8	Wilcoxon Rank	0.6676
Fig 4j	Object Sample AVG Z-score: nonTg vs. Tg	10 vs. 9	Wilcoxon Rank	0.0152*
Fig 5b	Home Cage CaT peak amplitude: nonTg vs. Tg	4 vs. 5	Wilcoxon Rank	0.8166
	Home Cage CaT frequency: nonTg vs. Tg	4 vs. 5	Wilcoxon Rank	0.8166
Fig 5d	Walk Peak Z-score: nonTg vs. Tg	4 vs. 5	Wilcoxon Rank	0.4832
	Walk AUC Z-score: nonTg vs. Tg	4 vs. 5	Wilcoxon Rank	0.3464
Fig 5f	nonTg AVG Z-score stem vs. D-zone	4	Paired t-test	0.0335*
	Tg AVG Z-score stem vs. D-zone	5	Wilcoxon Signed	1
	nonTg Peak Z-score stem vs. D-zone	4	Paired t-test	0.0333*
	Tg Peak Z-score stem vs. D-zone	5	Wilcoxon Signed	1
Fig 5h	Object-Zone AUC Z-score: nonTg vs. Tg	4 vs. 5	Wilcoxon Rank	0.7584
	Object-Zone RMS Z-score: nonTg vs. Tg	4 vs. 5	Wilcoxon Rank	0.0107*
Fig S1b	RI Sample: VIP-nonTg vs. VIP-Tg	10 vs. 11	Unpaired t-test	0.8373
	RI Test: VIP-nonTg vs. VIP-Tg	10 vs. 11	Unpaired t-test	0.0040**
Fig S1c	Total object exploration time (Test): VIP-nonTg vs. VIP-Tg	10 vs. 11	Unpaired t-test	0.1408
	Total horizontal activity (Test): VIP-nonTg vs. VIP-Tg	10 vs. 11	Unpaired t-test	0.0933
Fig S2c	sIPSC amplitude: VIP-nonTg vs. VIP-Tg	5, 7 vs. 5, 6	Unpaired t-test	0.4664
	sIPSC frequency: VIP-nonTg vs. VIP-Tg	5, 7 vs. 5, 6	Unpaired t-test	0.3349

	sEPSC amplitude: VIP-nonTg vs. VIP-Tg sEPSC frequency: VIP-nonTg vs. VIP-Tg	5, 5 vs. 4, 4 5, 5 vs. 4, 4	Unpaired t-test Unpaired t-test	0.2961 0.5242
Fig S3b	IS3 soma area: VIP-nonTg vs. VIP-Tg	5, 6 vs. 4, 5	Wilcoxon Rank	0.4818
Fig S3c	IS3 dend. surface: VIP-nonTg vs. VIP-Tg	5, 6 vs. 4, 5	Wilcoxon Rank	0.3773
Fig S3d	IS3 dend. length: VIP-nonTg vs. VIP-Tg	5, 6 vs. 4, 5	Wilcoxon Rank	0.3773
Fig S3e	IS3 dend. branch points: VIP-nonTg vs. VIP-Tg	5, 6 vs. 4, 5	Wilcoxon Rank	0.7258
Fig S3f	IS3 dend. length vs. distance from soma: VIP-nonTg vs. VIP-Tg IS3 dend.number of intersections vs. distance from soma: VIP-nonTg vs. VIP-Tg IS3 dend. number of nodes vs. distance from soma: VIP-nonTg vs. VIP-Tg	5, 5 vs. 4, 5 5, 5 vs. 4, 5 5, 5 vs. 4, 5	Two-way ANOVA Two-way ANOVA Two-way ANOVA	>0.9999 0.9941 >0.9999
Fig S4b	sEPSC amplitude: nonTg vs. Tg sEPSC frequency: nonTg vs. Tg	5, 8 vs. 4, 5 5, 8 vs. 4, 5	Wilcoxon Rank Wilcoxon Rank	0.3185 0.4789
Fig S4c	sEPSC rise time: nonTg vs. Tg sEPSC decay tau: nonTg vs. Tg sEPSC charge transfer: nonTg vs. Tg	5, 8 vs. 4, 5 5, 8 vs. 4, 5 5, 8 vs. 4, 5	Wilcoxon Rank Wilcoxon Rank Unpaired t-test	0.6722 0.7782 0.4585
Fig S5b	Home Cage CaT peak amplitude: nonTg vs. Tg Home Cage CaT frequency: nonTg vs. Tg	9 vs. 8 9 vs. 8	Wilcoxon Rank Wilcoxon Rank	0.3539 0.0915
Fig S5d	Locomotion Z-score: nonTg vs. Tg Immobility Z-score: nonTg vs. Tg Rearing Z-score: nonTg vs. Tg	9 vs. 8 9 vs. 8 9 vs. 8	Wilcoxon Rank Wilcoxon Rank Wilcoxon Rank	0.4257 0.8721 0.2259
Fig S5e	DZ average speed: nonTg vs. Tg DZ average mobility speed: nonTg vs. Tg DZ distance traveled: nonTg vs. Tg	10 vs 5 10 vs 5 10 vs 5	Wilcoxon Rank Wilcoxon Rank Wilcoxon Rank	0.7229 0.1462 0.2298
Fig S5f	Stem average speed: nonTg vs. Tg Stem average mobility speed: nonTg vs. Tg Stem distance traveled: nonTg vs. Tg	10 vs 5 10 vs 5 10 vs 5	Wilcoxon Rank Wilcoxon Rank Wilcoxon Rank	0.6359 0.2298 0.6359

Supplementary figures.

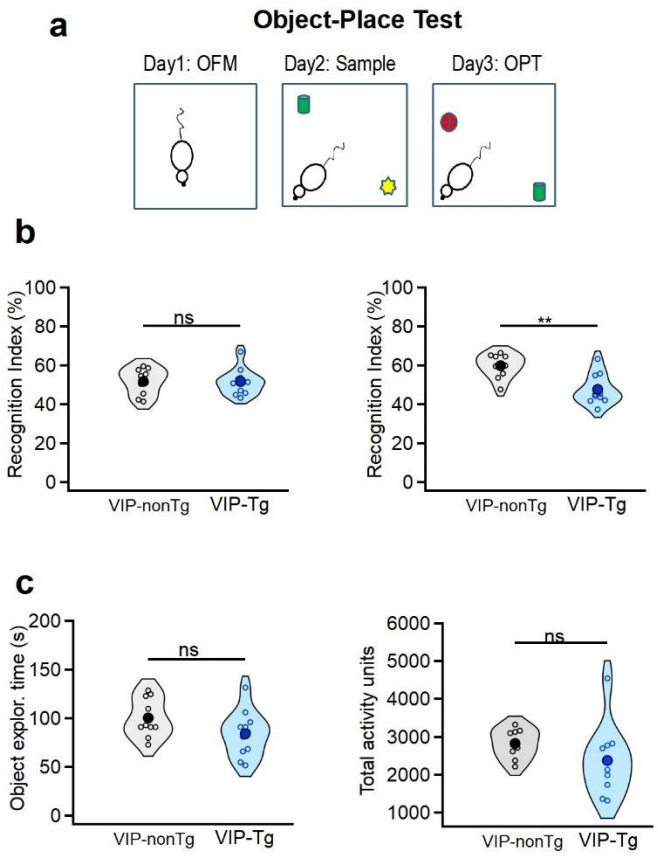

Supplementary figure 1. Early deficits in the object-place test of VIP-Tg mice.

a. Schematic for the object-place test (OPT): Day 1 – open field maze (OFM) exploration; Day 2 – Sampling of two different objects; Day 3 – OPT, in which one of the objects has been replaced by a new one and the second was displaced. In this test, mice show preference for a novel object (Francavilla et al., 2020). **b.** Summary plots showing the recognition index (RI) on day 2 (left) and on day 3 (right) for VIP-nonTg and VIP-Tg mice. **$p<0.01$ (VIP-nonTg: n = 10 animals; VIP-Tg: n = 11 animals). **c.** Summary plots showing the total object exploration time on day 3 (left) and the total horizontal activity (right) for VIP-nonTg and VIP-Tg mice (VIP-nonTg: n = 10 animals; VIP-Tg: n = 11 animals). Note a significant decrease of RI in VIP-Tg mice despite unaltered activity and total exploration time.

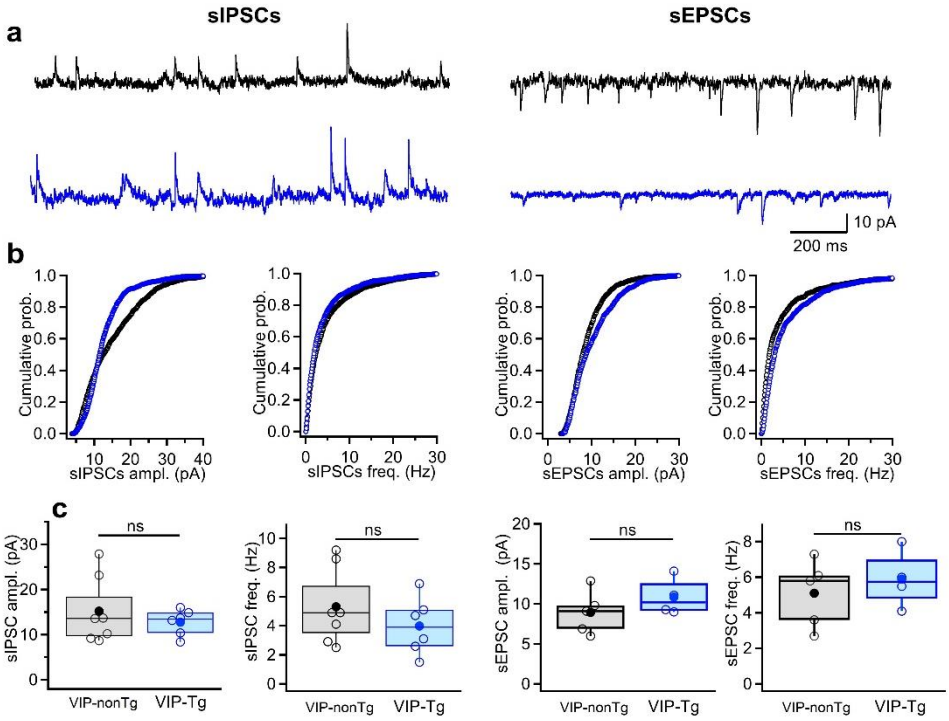

Supplementary Figure 2. Unaltered synaptic drive to I-S3 cells in VIP-Tg mice.

a. Representative traces for spontaneous inhibitory (sIPSCs, left) and excitatory (sEPSCs, right) postsynaptic currents in I-S3 cells from VIP-nonTg (top, black) and VIP-Tg (bottom, blue) mice. **b.** Summary plots showing the cumulative probability for sIPSCs amplitude (left) and frequency (middle left) as well as the sEPSCs amplitude (middle right) and frequency (right) in I-S3 cells from VIP-nonTg (black) and VIP-Tg (blue) groups. **c.** Summary plots showing the animal-wise data for sIPSCs (VIP-nonTg: n = 7 cells/5 animals; VIP-Tg: n = 6 cells/5 animals) amplitude (left) and frequency (middle left) as well as the sEPSCs (VIP-nonTg: n = 5 cells/5 animals; VIP-Tg: n = 4 cells/4 animals) amplitude (middle right) and frequency (right) in I-S3 cells.

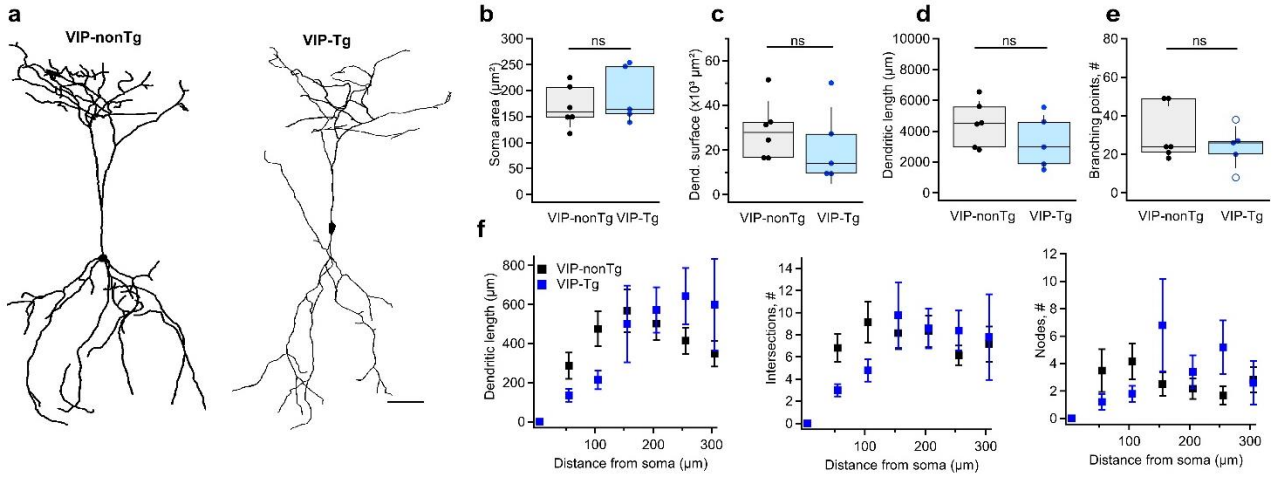

Supplementary Figure 3. Unaltered morphological properties of I-S3 cells in VIP-Tg mice. **a.** Anatomical reconstructions of I-S3 cells filled with biocytin from VIP-nonTg (left) and VIP-Tg (right) animals. Scale bar: 50 µm. **b-e.** Summary plots showing the soma area (b), the total dendritic surface (c), the dendritic length (d), and the number of dendritic branching points (e) of I-S3 cells for VIP-nonTg and VIP-Tg groups (VIP-nonTg: n = 6 cells/5 animals; VIP-Tg: n = 5 cells/4 animals). **f.** Sholl analysis of the dendritic length (left), number of intersections (middle) and number of dendritic nodes (right) in relation to the distance from the soma in I-S3 cells for VIP-nonTg and VIP-Tg groups (VIP-nonTg: n = 5 cells/5 animals; VIP-Tg: n = 5 cells/4 animals).

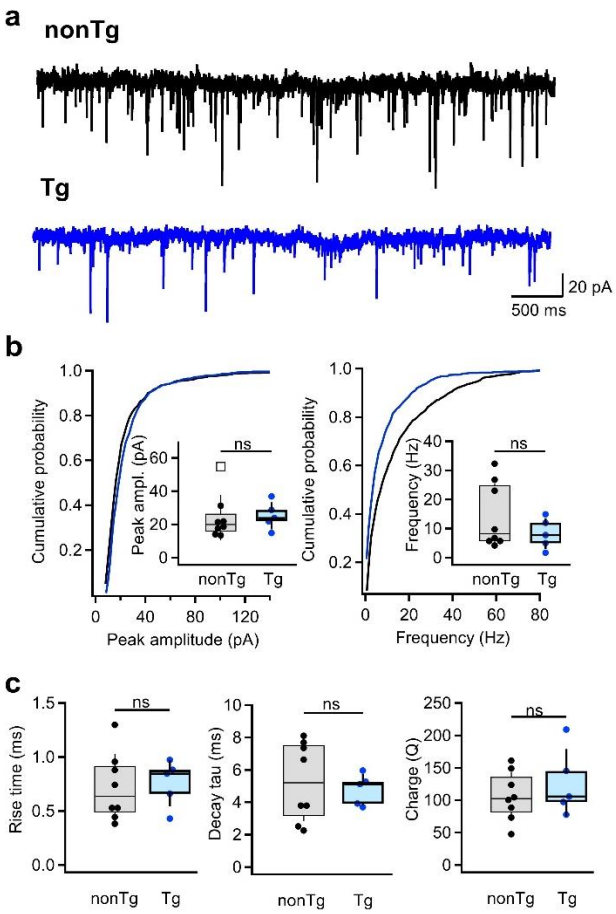

Supplementary Figure 4. Excitatory drive to O/A INs remains unchanged in Tg mice.

a. Representative traces for sEPSCs in O/A INs from nonTg (top, black) and Tg (bottom, blue) mice. **b.** Summary distribution plots showing the sEPSCs amplitude (left) and frequency (right). Insets show summary data for animal-wise comparison (nonTg: n = 8 cells/5 animals; Tg: n = 5 cells/4 animals). **c.** Summary boxplots showing the rise time (left), decay time constant (middle), and charge transfer (right) for sEPSCs (nonTg: n = 8 cells/5 animals; Tg: n = 5 cells/4 animals).

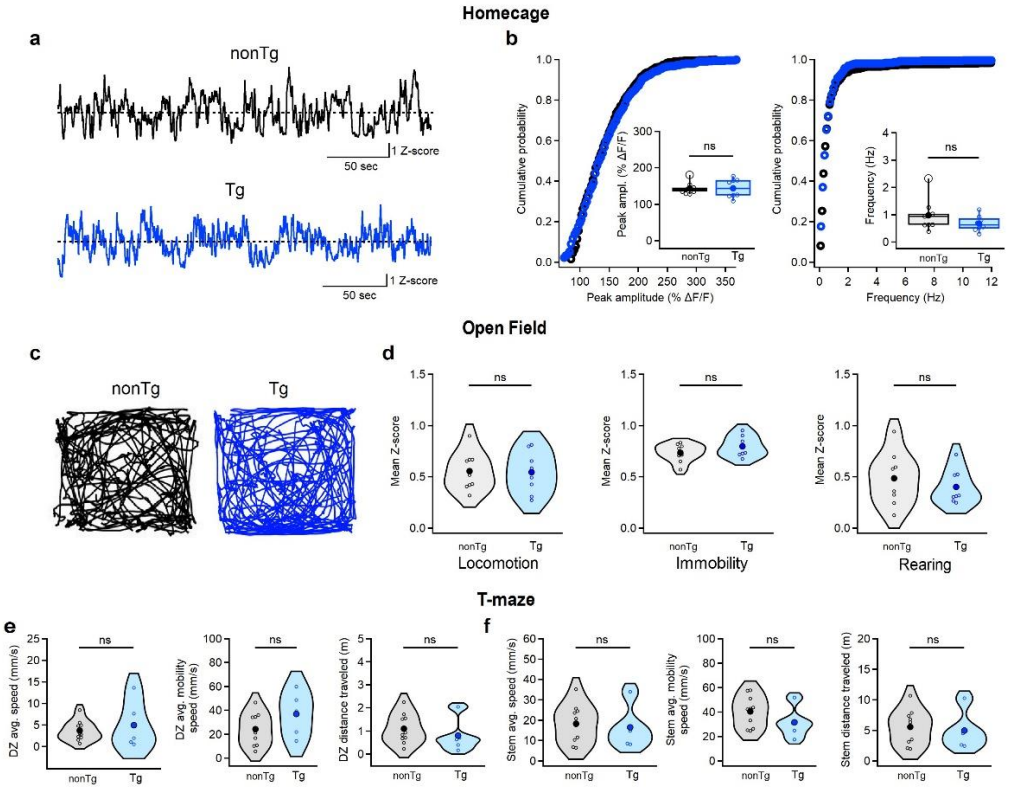

Supplementary Figure 5. Unaltered activity of CA1 interneurons in home cage and open field and unchanged mobility in T-maze.

a. Representative calcium traces from CA1 O/A INs in nonTg (black) and Tg (blue) mice recorded when animals were in their homecage. **b.** Summary plots showing the peak amplitude (left) and frequency (right) of calcium transients in O/A INs in non-Tg (black) and Tg (blue) animals in their homecage. Insets show boxplots for animal-wise mean comparison (nonTg: n = 9 animals; Tg: n = 8 animals). **c.** Representative movement trajectories during OFM for non-Tg (left, black) and Tg mice (right, blue). **d.** Summary plots showing the animal-wise comparison for the mean Z-scored values of calcium transients during periods of locomotion (left), immobility (middle) and rearing (right) in the OFM (nonTg: n = 9 animals; Tg: n = 8 animals). **e.** Summary plots showing the average speed (left), average mobility speed (middle) and total distance traveled (right) in the DZ of the T-maze (nonTg: n = 10 animals; Tg: n = 5 animals) in nonTg (black) and Tg (blue) animals. **f.** Summary plots showing the average speed (left), average mobility speed (middle) and total

distance traveled (right) in the stem part of the T-maze (nonTg: n = 10 animals; Tg: n = 5 animals) in nonTg (black) and Tg (blue) animals.